NEAR EARTH OBJECT DETECTION USING A POISSON STATISTICAL

MODEL FOR DETECTION ON IMAGES MODELED FROM THE

PANORAMIC SURVEY TELESCOPE & RAPID RESPONSE SYSTEM

THESIS

Curtis J. R. Peterson, Captain, USAF

AFIT/GE/ENG/12-33

DEPARTMENT OF THE AIR FORCE
AIR UNIVERSITY

AIR FORCE INSTITUTE OF TECHNOLOGY

Wright-Patterson Air Force Base, Ohio

AFIT/GE/ENG/12-33

NEAR EARTH OBJECT DETECTION USING C'POISSON STATISTICAL MODEL FOR DETECTION ON IMAGES MODELED FROM THE PANORAMIC SURVEY TELESCOPE & RAPID RESPONSE SYSTEM

THESIS

Presented to the Faculty

Department of Electrical and Computer Engineering

Graduate School of Engineering and Management

Air Force Institute of Technology

Air University

Air Education and Training Command

In Partial Fulfillment of the Requirements for the

Degree of Master of Science in Electrical Engineering
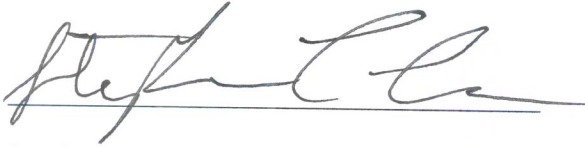
Curtis J. R. Peterson,

Captain, USAF

March 2012

AFIT/GE/ENG/12-33

NEAR EARTH OBJECT DETECTION USING POISSON STATISTICAL MODEL FOR DETECTION ON IMAGES MODELED FROM THE PANORAMIC SURVEY TELESCOPE & RAPID RESPONSE SYSTEM

Curtis J. R. Peterson,

Captain, USAF

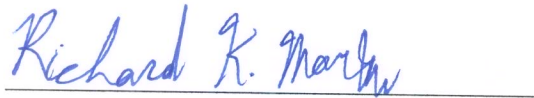Approved:

_____   29 Feb 2012
Stephen C. Cain, PhD (Chairman)   Date

_____   29 Feb 2012
Richard Martin, PhD (Member)   Date

_____   29 Feb 2012
Patrick Chapin, Maj, PhD, USAF (Member)   Date

Abstract

The purpose of this research effort is to develop, simulate, and test a new algorithm to detect Near Earth Objects (NEOs) using a Likelihood Ratio Test (LRT) based on a Poisson statistical model for the arrival of photons. One detection algorithm currently in use is based on a Gaussian approximation of the arrival of photons, and is compared to the proposed Poisson model. The research includes three key components. The first is a quantitative analysis of the performance of both algorithms. The second is a system model for simulating detection statistics. The last component is a collection of measured data to apply comparatively to both algorithms.

A Congressional mandate directs NASA and the DoD to catalogue 90% of all NEOs by the year 2020 [1]. Results from this research effort could feasibly be applied directly to operations in the Pan-Starrs program to facilitate the accomplishment of the Congressional mandate. Improvements in the size of detectable NEOs and in the probability of detecting larger NEOs would increase the state of readiness of the world for possible catastrophic impact events. Improvements in detection probability of measured data were as high as a factor of seven, and the expected average improvement is 10%.

Acknowledgments

      I would like to express my sincere appreciation to my family and friends for their continued support, encouragement and understanding. I would also like to thank my AFIT professors, especially my research advisor, Dr. Stephen Cain for their guidance, instruction, and patience throughout my Master's program and the research process.

<div align="center">Curtis J. R. Peterson</div>

Table of Contents

List of Figures

List of Tables

NEAR EARTH OBJECT DETECTION USING POISSON STATISTICAL

MODEL FOR DETECTION ON IMAGES FROM THE PANORAMIC SURVEY

TELESCOPE & RAPID RESPONSE SYSTEM

1   Introduction

1.1   General Issue

In the National Aeronautics and Space Administration (NASA) Multiyear Authorization Act of 1990, the United States Congress directed a workshop study to define a program to increase the detection rate of asteroids whose trajectory crosses the orbital path of Earth. This lead to NASAs Spaceguard Survey Report in 1992, the conclusions of which called for a worldwide network of 4 to 7 telescopes in the 2 to 3 meter aperture range. The report predicted that nearly all asteroids and comets over 1 km in diameter could be catalogued and tracked with such a network. The report predicts that 10 percent of smaller asteroids and comets between 100 meters and 1 km in diameter could be catalogued and tracked with a similar system. The report outlines the need for cooperation with the Department of Defense, particularly with the US Air Force, in the search for NEOs [2].

In 1994, the House Committee on Science and Technology directed NASA, in coordination with the Department of Defense and other international space agencies to discover, catalogue, and track within 10 years, 90 percent of all asteroids and comets larger than 1 km within 1.3 Astronomical Units (AU) from the sun whose trajectory crosses the orbital path of Earth. Eleven years later, the NASA Authorization Act of

2005 issued a new mandate in which 90% of all NEOs larger than 140 meters in diameter must be discovered, catalogued, and tracked by the year 2020. Congress also directed NASA to submit an Analysis of Alternatives (AoA) to the Committee within 120 days of enactment of the Act, outlining efforts taken by NASA to detect and characterize the hazards of NEOs, as well as an assessment of necessary actions to put in place capabilities to expand detection and tracking of NEOs [1].

The AoA submitted to Congress by NASA in 2007 details two considered terrestrial detectors, and several space-based systems. The two terrestrial based systems are the Large Synoptic Survey Telescope (LSST), and Panoramic Survey Telescope and Rapid Response System (Pan-Starrs) [3]. The AoA reported that a program consisting of a combination of both ground based systems and some space-based systems was required to meet the 2020 deadline for completion. The AoA also reported that using only one of the land-based systems would push the date out to beyond 2030. The number of NEOs estimated by the AoA is depicted in Figure 1, using a constant power law [3].
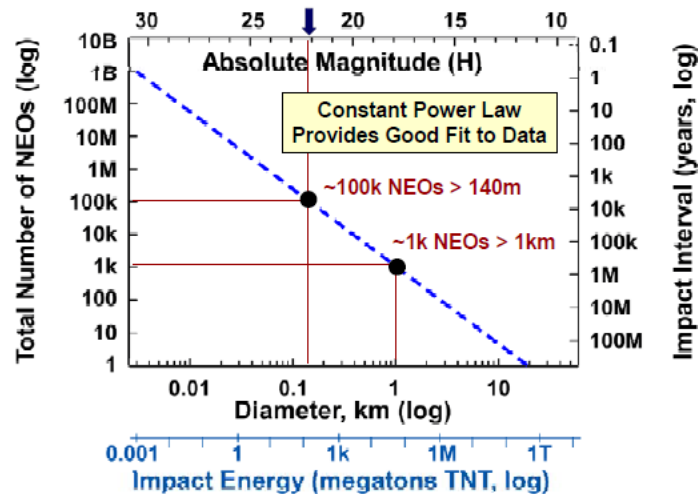
Figure 1. Frequency of NEOs by Size, Impact Energy, and Magnitude **[3]**
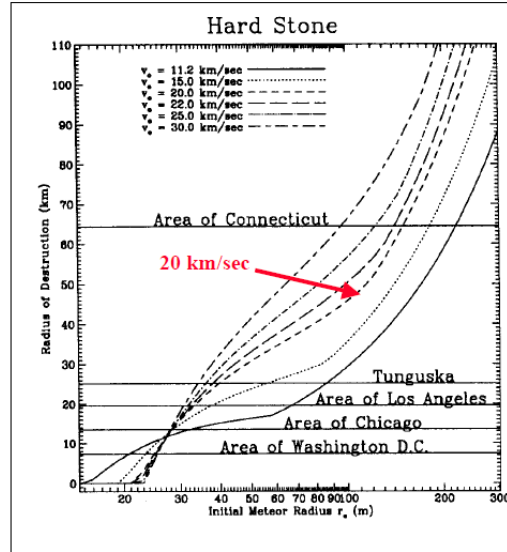
Figure 2. Impact Destruction Radius **[4]**

Large NEOs have an impact frequency of one every half a million years, while sub-kilometer NEOs impact one in every thousand years [4]. While the probability of an impact of a large NEO capable of triggering mass extinctions within a lifetime is small, the probability of an impact from a smaller NEO is significantly higher, and as Figure 2 illustrates, such an impact would cause catastrophic localized damage.

1.2   Problem Statement

NASA's budget request for NEO observations rose from $5.8M in FY 2010 to $20.4M in FY 2011 and beyond, the largest increase since NASA began searching for NEOs [5]. This increase reflects the realization that enough is not being done to accomplish the Congressional Mandate outlined in [1]. The cost for the spaced-based systems outlined in [3] was forecasted to be more than twice that of the terrestrial-based systems, as well as being more complicated to support and maintain. The cost of the terrestrial-based systems was forecasted to be $469M and would not meet the

3
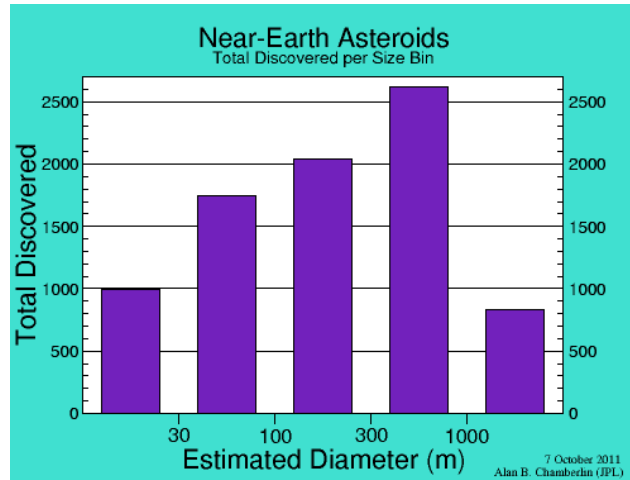
Figure 3. Total NEO Discoveries **[6]**

requirements of the mandate until the year 2026 [3]. As of 7 October 2011, fewer than 900 NEOs larger than 1 km have been discovered, and fewer than 5000 between 100 m and 1 km have been discovered, as shown in Figure 3 [6]. With the given operating budget for NEO detection, the required budget, and the current progress of the effort to complete the Congressional mandate, a solution is needed that improves the detection capability of current equipment at minimal costs.

1.3   Research Objectives/Focus

The objectives of this research effort will be to develop a new algorithm for detecting NEOs using existing hardware, namely Pan-Starrs. The research will be focused on decreasing the detectable size and increasing the probability of detecting larger NEOs by changing the post-processing algorithm of image data. The model for the simulations will be greatly simplified from the complex algorithm that is currently in use. All of the functionality of Pan-Starrs is not investigated in this report; therefore, only the process by which Pan-Starrs takes image data and uses it to flag the detection of a NEO is

modeled. Likewise, the investigated algorithm would likely require additional functionality and integration work in order to implement.

1.4 Investigative Questions

How does Pan-Starrs currently detect NEOs? What are the optical capabilities of Pan-Starrs? Given the capabilities of the Pan-Starrs hardware, what detection theory can be applied to the post-processing of the image data? How does any proposed detection algorithm compare to the existing detection algorithm? Can any proposed algorithm extend to applications other than Pan-Starrs?

1.5 Methodology

Receiver Operating Characteristic (ROC) curves will be generated through Monte Carlo simulations based on models of the Pan-Starrs optical characteristics, atmospheric characteristics, and NEO characteristics. Simulations of varying environments such as proximity to brighter objects, and the intensity of nearby objects will be investigated. Tests in relative environments will be conducted to verify the results of the simulations.

1.6 Assumptions/Limitations

Many variables are involved in the ability to detect a NEO. Without actual data from Pan-Starrs, assumptions must be made about the environment in which images will be taken. Average atmospheric conditions, average NEO characteristics, and the average optical response of Pan-Starrs will be used in the simulations. Similarly, without the availability of Pan-Starrs hardware, a relative test environment will be derived based on the results seen in simulations.

1.7   Implications

Results from this research effort could feasibly be applied directly to operations at Pan-Starrs and other programs. If improvements in the size of detectable NEOs or in the probability of detecting larger NEOs are observed, the algorithm could be used to facilitate the accomplishment of the Congressional mandate to have 90% of all NEOs over 140 m in diameter catalogued by 2020.   Any such notable improvement would increase the state of readiness of the world for possible catastrophic impact events.

1.8   Preview

This research aims to demonstrate that detection theory can be used to implement a Likelihood Ratio Test (LRT) to improve upon the current detection algorithm used by Pan-Starrs.   Further, it aims to demonstrate that other known electronic filtering techniques are based on approximations about the stochastic nature of photon-counting and that improved results are possible without making such approximations. Chapter 2, Literature Review, compares the previous, current and planned NEO detection methods of multiple NEO detection programs.   Chapter 3, Methodology, details the analytic process that led to the proposed algorithm, as well as the approach used to develop models, simulations, and tests. Chapter 4, Analysis and Results, interprets the outcomes of the analysis, simulations, and tests.   Chapter 5, Conclusions and Recommendations, discusses the validity and performance of the proposed algorithm based on comparisons of the analytical, simulation and test outcomes with the performance of current NEO detection methods.

2   Literature Review

2.1   Chapter Overview

The purpose of this chapter is to review past, current, and future NEO detection methods. Beginning in 1984 with the Spacewatch program, through the estimated 2020 operational date of the Large Synoptic Survey Telescope (LSST) program there have been numerous government and academic programs dedicated, at least in part, to the discovery and cataloguing of NEOs. An analysis of the algorithms and system capabilities of such programs will show that the proposed algorithm in this research effort is a novel approach to the post-processing of astronomical image data. NEO detection programs have employed increasingly more capable and sophisticated optical systems and computer processing systems; however, very little has changed in the basic method of detecting NEOs.

2.2   Previous and Current Programs

In 1984, University of Arizona's Spacewatch program became the first to use Charge-coupled Devices (CCDs) to scan the sky for NEOs. The Spacewatch team developed the tools and methods used by many of the astronomical observing telescopes today to automatically detect moving objects using CCDs [7]. The "drift-scan" method focuses the telescope at a point slightly leading the targeted area and keeps it stationary, allowing the sky to drift across the field of view due to the rotation of the Earth. The read out rate of the CCD is set equal to the drift rate of the sky, providing a very long exposure time while keeping any fixed objects in focus. Objects that are moving fast relative to the background sky, as NEOs would be, would appear as streaks in the image. The "step-

stare" method uses a mosaic of fast read out CCDs to piece together an image then return to the same area of sky a number of times within a small timeframe in order to perform some type of change detection between the two images. NEOs moving faster than the background sky, instead of appearing as streaks, will appear in a different location relative to the surrounding objects in the image [8].

Since the Spacewatch program, at least five subsequent NEO detection programs have used, or are using the "step-stare" method in order to detect moving objects. These programs include the Near Earth Asteroid Tracking (NEAT), Lincoln Near Earth Asteroid Research (Linear), Lowell Observatory NEO Search (LONEOS), Catalina Sky Survey (CSS), and the Japanese Spaceguard Association (JSGA) programs. Each of these programs has offered unique capabilities and contributions, but a detailed review of each program is outside of the scope of this document [9] Table 1 displays a summary comparison of the six program telescopes previously discussed [8].

Table 1. Comparison of current NEO search programs

Program	Space-watch1	Space-watch2	NEAT-1	NEAT-2	LONEOS	LINEAR	Catalina Sky Survey	JSGA
Aperture (m)	0.9	1.8	1.2	1.2	0.6	1	0.4	0.5
f #	5.3	2.7	1.9	2.5	1.9	2.2	3	1.9
Pixel Size (mm)	0.024	0.024	0.015	0.015	0.0135	0.024	0.015	0.015
Pixel Size (arcsec)	1	1	1.4	1	2.5	2.25	2.5	3.2
FOV (deg^2)	0.3	0.3	2.5	3.8	8.3	2	8.1	3.1
Readout Mode	drift scan	ds/step stare	step stare	step stare	step stare	step stare	step stare	step stare
Exposure (sec)	150	150	20	60	45	5	60	23
Revisits	3	3	3	3	4	5	4	-

2.3 Future Programs

As stated in Chapter 1, two proposed future efforts, Pan-Starrs and LSST, were detailed in the AoA submitted to Congress by NASA in 2007 [3]. Since the submittal of the AoA, plans for both future programs have matured significantly. The LSST scheduled first light is in 2018 and no hardware has yet been delivered [10]. The first of four identical pieces of Pan-Starrs, PS1 has been installed on Haleakala, in Hawaii and has been officially conducting scientific observations since May 2010. PS1 will be used to test the design and technology being developed for Pan-Starrs. The second piece, PS2, is scheduled for installation in early 2013. The installation of the remaining pieces is currently unscheduled [11]. Pan-Starrs has implemented the first major change in NEO detection methods, and no longer looks for moving objects based on two single images that are both susceptible to noise. Instead, Pan-Starrs creates a running average, or "master image" of the sky and uses it in an image differencing algorithm. The availability of the master image is the genesis of this research effort and for this reason the remainder of the focus of this section will be the review of literature as it pertains to the methods and capabilities of Pan-Starrs and how the Pan-Starrs program conducts NEO surveillence.

2.4 Pan-Starrs Specifications

PS1 has a 1.8 meter diameter concave primary mirror and an effective focal length of 8 meters. The camera on the PS1 is an 8 by 8 array of CCD devices approximately 5 cm^2 each. The individual devices are made up of an 8 by 8 array of CCD cells with almost 600 by 600 pixels per cell, providing approximately 1.4 Giga-
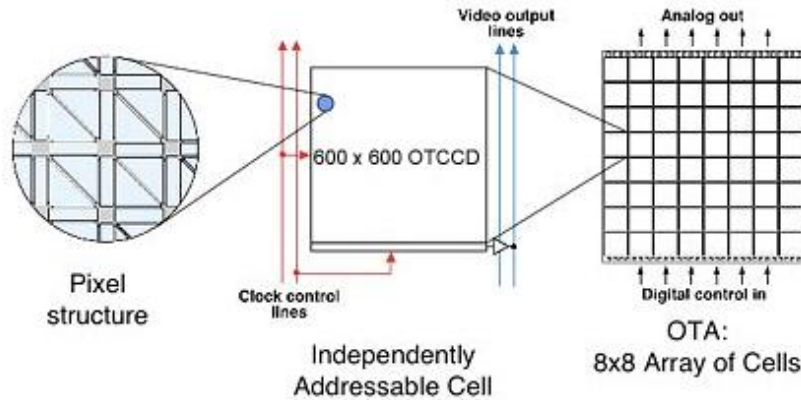
Figure 4. Pan-Starrs CCD Structure **[11]**

pixels total, as illustrated in Figure 4.   The pixel resolution of the 10 μm pixels is approximately 0.258 arcsec [11].

PS1 can utilize one of several filters depending on the application.   For NEO observations, a wideband 0.5 to 0.8 μm filter will typically be used. With the wideband filter, sky background noise is expected to be approximately 7 electrons per pixel, while the read noise in the CCD cells is expected to be about 5 electrons.   Typical exposure times will be 30 seconds, in which about seven square degrees of the sky will be imaged [11].

When the full Pan-Starrs is operational, images from each of the four telescopes will be compared and combined into a composite image providing resilience to cosmic rays, error due to gaps between CCD cells, and bad pixels. Any composite image that is found to have no objects of interest will be used to build up the running master image of the sky. New composite images will be analyzed for objects above a certain intensity threshold, which will be stored in a database for future reference. New images may

optionally be smoothed with a modeled Point Spread Function (PSF) estimated from the image and will be subtracted from the cumulative master image leaving only images of objects that have moved or changed intensity [12]. The images remaining will be added to a separate database for further review. Finally, the composite image is discarded to free up data storage [11].

2.5   Relevant Research

Research conducted in 2004 and published in the October 2005 issue of *The Astronomical Journal*, "Matched Filter Processing for Asteroid Detection" described methods to implement a matched filter algorithm for the specific application of near Earth asteroid detection [13]. The results of this paper showed a 40 percent increase in asteroid detection rates compared to the "step stare" and "drift scan" algorithms [13]. A paper published in *The Astronomical Journal* in 2005, "Likelihood-Based Method for Detecting Faint Moving Objects" develops a Maximum Likelihood Estimate of the magnitude and velocity of dim moving objects given the photon distribution received from a 5 minute exposure time [14]. The results of this research showed improvement in the detectable magnitude of objects for a given telescope, but the process requires extremely long exposure times, multiple images, and a significant amount of computational time [14].

Another research effort, "Detecting Near-Earth Objects Using Cross-Correlation with a Point Spread Function" was conducted at AFIT and focused on the Linear program telescope [15]. The results of this research found that the Linear program would improve detection by using electronic matched filtering and proper sampling [15]. Pan-Starrs has

an optional setting to smooth the difference image with a modeled PSF, in other words to perform matched filtering. Sampling turns out not to be an issue with Pan-Starrs as it was with Linear. The Nyquist sampling theorem dictates that the Pan-Starrs detector is sampled as

$$\Delta_s \leq \frac{\lambda f}{2D} = \frac{(0.5 \times 10^{-6} \, meters)(8 meters)}{2(1.8 meters)} \cong 1.11 \mu m \,, \tag{1}$$

where Δ_s is the sample spacing, λ is the wavelength, f is the focal length, and D is the aperture diameter [16]. Although it appears that the $10 \mu m$ physical pixel size is under sampling by a factor of nearly 10, the cutoff frequency due to the atmosphere is much lower. Fried's seeing parameter, r_0, is a measure of the strength of the turbulence in the atmosphere and has the effect of limiting the effective diameter of the system, if the diameter is larger than r_0. As shown in Figure 5, the average r_0 at Haleakala, the location of PS1, is approximately 9 cm during hours of darkness [17].
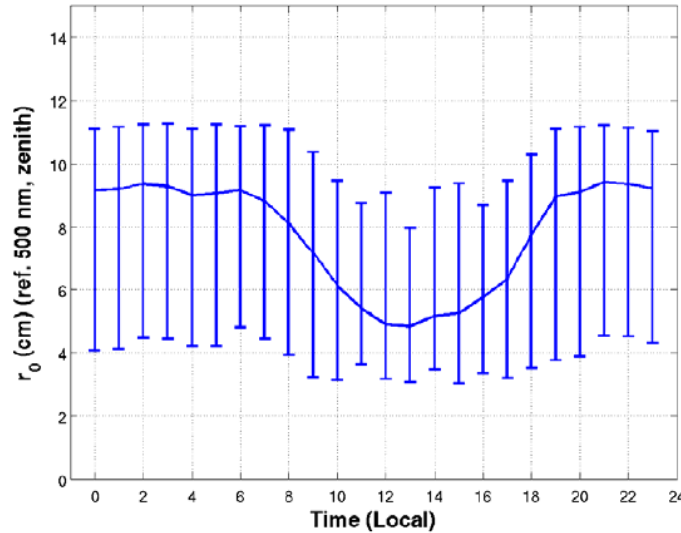
Figure 5. Average hourly r_0 for Haleakala, May-Oct

This means that r_0 is the limiting factor in the spatial resolution of the PS1 system, and using 9 cm for D in Eq. (1) yields a minimum effective spatial sampling of

$$\Delta_s \leq \frac{\lambda f}{2r_0} = \frac{\left(0.5 \times 10^{-6} meters\right)\left(8 meters\right)}{2\left(0.09 meters\right)} \cong 22.2 \mu m,$$

which means that the $10 \mu m$ physical pixel size of PS1 is sampling at a rate about twice that which is necessary for the average atmosphere and is fine enough sampling for an r_0 of up to 20 cm.

2.6   Summary

Six of the largest NEO detection programs over the last 25 years all use the same fundamental approach.   The newest program, Pan-Starrs, introduces the method of producing an average image of the sky and using that image for difference detection in order to identify new objects that are not typically in that image.   Not much has been reported about the LSST program due to the stage of development.   LSST plans on using both the step-stare and image difference detection.   Instead of building their own master image, the plan calls for a star chart used in a similar manner as Pan-Starr's master image [10].   The availability of Pan-Starr's master image provides a statistical tool, the expected value of the sky image, which may be utilized in a classical signal detection approach using a Likelihood Ratio Test, a method that has not been applied to the NEO detection problem.   The proposed algorithm removes assumptions about the statistical nature of photon arrival and implements a LRT detection scheme.   The new algorithm requires the master image, but uses it as the statistical mean of an image taken with the Pan-Starrs camera as opposed to generating a difference image.

3   Methodology

3.1   Chapter Overview

The results of [15] showed that a matched filter, or a cross-correlation with the PSF, would improve NEO detection using the Linear telescope. This chapter will show that using the PSF smoothing option of the Pan-Starrs system on the differenced image is actually applying an assumption that the photon noise is both white and Gaussian. Eliminating this assumption is the basis for the research effort. A detailed explanation follows that describes the analytical, simulation, and measurement tools used to develop and demonstrate a more effective detection algorithm based on photons having a Poisson distribution. The analytical tools include a derivation of the signal to noise ratio (SNR) as a metric to compare the algorithms. Simulation tools include the development of the complete model of the Pan-Starrs equipment, atmosphere and astronomical objects. Measured tools include the development of a relative test environment to recreate conditions that will be seen in practical applications of the algorithms.

3.2   Photon Statistics

Detecting the presence of an object optically is done by measuring the number of photons received at the detector from the object. There will also be photons arriving from the ambient background radiation of the scene. Detecting the object requires a statistical characterization of the arrival of all photons in order to distinguish between photons from a target object and those from background radiation. Assume a total of N photons are emitted over time in any one direction from an isotropic source. The rate, $\lambda(t)$, at which n photons arrive in t seconds at the detector would be

$$\lambda(t) = \frac{n}{t}\left(photons\middle/ s\right).$$

The probability, p of a photon arriving in a time interval (t_1, t_2) is simply [18]

$$p = \int_{t_1}^{t_2} p_\lambda(t)dt,$$

where $p_\lambda(t)$ is the probability density, or the photon arrival probability per second. Intuitively, the probability density is proportional to the arrival rate for photons, or

$$p_\lambda(t) \propto \lambda(t).$$

The probability density must integrate to one; therefore,

$$p_\lambda(t) = \frac{n}{Nt}\left(\frac{P[\text{photon arriving}]}{s}\right), \text{ or}$$

$$p_\lambda(t) = \frac{\lambda(t)}{N}\left(\frac{P[\text{photon arriving}]}{s}\right).$$

The arrival of K_N photons from a source of N photons in a time interval (t_1, t_2) can be characterized as a binomial random variable with N total experiments, K_N successes, and a probability of success of p. The probability, $P(K_N)$ of K_N photons arriving in the interval (t_1, t_2) is then,

$$P(K_N) = \binom{N}{K}p^{K_N}(1-p)^{N-K_N}, \tag{2}$$

$$= \frac{N!}{(N-K)!K_N!}\left[\int_{t_1}^{t_2}\frac{\lambda(t)}{N}dt\right]^{K_N}\left[1 - \int_{t_1}^{t_2}\frac{\lambda(t)}{N}dt\right]^{N-K_N},$$

$$= \frac{N(N-1)\cdot\ldots\cdot(N-K_N+1)(N-K_N)!}{(N-K_N)!K_N!}\left[\frac{1}{N}\int_{t_1}^{t_2}\lambda(t)dt\right]^{K_N}\left[1 - \frac{1}{N}\int_{t_1}^{t_2}\lambda(t)dt\right]^{N-K_N},$$

15

$$= \frac{N(N-1)\cdot...\cdot(N-K_N+1)}{K_N!N^{K_N}}\left[\int_{t_1}^{t_2}\lambda(t)dt\right]^{K_N}\left[1-\frac{1}{N}\int_{t_1}^{t_2}\lambda(t)dt\right]^{N-K_N}.$$

The total number of photons emitted from a source, N can be assumed to be uncountable and large; therefore,

$$P(K_N)=\lim_{N\to\infty}\left\{\frac{N(N-1)\cdot...\cdot(N-K_N+1)}{K_N!N^{K_N}}\left[\int_{t_1}^{t_2}\lambda(t)dt\right]^{K_N}\left[1-\frac{1}{N}\int_{t_1}^{t_2}\lambda(t)dt\right]^{N-K_N}\right\},\quad(3)$$

and when N is large, [19]

$$\left[1-\frac{1}{N}\int_{t_1}^{t_2}\lambda(t)dt\right]^{N-K_N}\approx\left[1-\frac{1}{N}\int_{t_1}^{t_2}\lambda(t)dt\right]^{N}\approx e^{-\int_{t_1}^{t_2}\lambda(t)dt}.$$

Eq. (3) simplifies to

$$P(K_N)\approx\lim_{N\to\infty}\left\{\frac{N(N-1)\cdot...\cdot(N-K_N+1)}{K_N!N^{K_N}}\right\}\left[\int_{t_1}^{t_2}\lambda(t)dt\right]^{K_N}e^{-\int_{t_1}^{t_2}\lambda(t)dt},$$

$$\approx\frac{1}{K_N!}\left[\int_{t_1}^{t_2}\lambda(t)dt\right]^{K_N}e^{-\int_{t_1}^{t_2}\lambda(t)dt}.\qquad(4)$$

The average number of photons, $\bar{K}_N$ arriving from a source of N photons in the time interval (t_1,t_2) is

$$\bar{K}_N=\int_{t_1}^{t_2}\lambda(t)dt;\qquad(5)$$

therefore, Eq. (4) becomes

$$P(K_N)\approx\frac{\bar{K}_N^{K_N}e^{-\bar{K}_N}}{K_N!},\qquad(6)$$

16

which is the Probability Mass Function for a Poisson random variable. This random variable is characterized by a single parameter which is equal to both the mean and the variance [20].

The range between the detector and the object, and the source of the photons from an object determines how the expected number of photons arriving at the detector is estimated. A NEO, within 1.3 AUs of Earth, is relatively close compared to a distant star light-years away. NEOs are also not the source of photons; rather they reflect photons from other sources. The expected number of photons, $\bar{K}_N$, received and converted into photo-electrons by the detector from a NEO illuminated only by natural light can be calculated using Eq. (7) [16].

$$\bar{K}_N = \frac{S_{IB}\Delta_\lambda A_B \rho_t \eta \tau_a \tau_o D^2 \lambda \Delta t}{4R^2 hc} \tag{7}$$

where:

- S_{IB} is the solar spectral irradiance incident on the NEO in Watts (J/s) per square meter per micro-meter,

- Δ_λ is the bandwidth of the filter in micro-meters,

- A_B is the two-dimensional surface area of the NEO that is normal to the optical axis in square meters,

- ρ_t is the dimensionless reflectivity of the NEO,

- η is the quantum efficiency of the detector in photo-electrons per photon,

- τ_a is the dimensionless transmittance of the atmosphere,

- τ_o is the dimensionless transmittance of the optical system,

- D is the diameter of the receiver aperture in meters,

- λ is the photon wavelength in meters,

- Δt is the exposure time in seconds,

- R is the range to the NEO in meters,

- h is Planck's constant in Joule seconds per photon, and

- c is the speed of light in meters per second.

      The natural light incident on the NEO is almost entirely from the Sun. The solar spectral irradiance at the top of Earth's atmosphere, shown in Figure 6, is used because it closely predicts the irradiance incident on a NEO without an atmosphere in an orbit close to the Earth's. The bandwidth of the wideband filter typically used for NEO detection by Pan-Starrs is 0.3 μm; however, this model will simulate the monochromatic response over the range of the filter in 0.1 μm increments, so 0.1 μm is used for Δ_λ, and
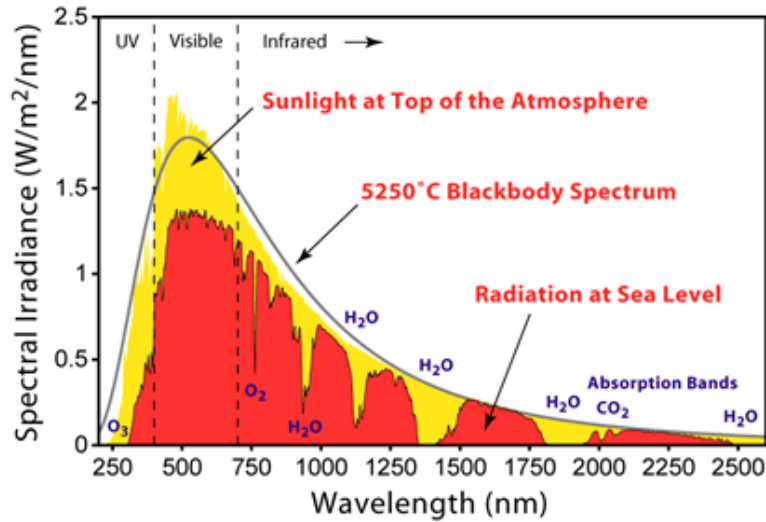
Figure 6. Solar Radiation Spectrum **[21]**

0.5 μm, 0.6 μm, 0.7 μm, and 0.8 μm will be used for λ. Four wavelength dependent values corresponding to each λ found in Figure 6 will be used for S_{IB}. The irregular and

unknown shape of a NEO makes using exact values for A_B impossible; therefore a circular surface will be assumed and the equation for the area of a circle with a diameter greater than or equal to 140 meters will determine the value used for A_B. This is a reasonable assumption because the variation in angular size on the detector plane between an irregularly shaped object and a spherical object is not measurable. NEOs are expected to have a reflectivity greater than 3 percent, which provides a lower bound on the value of ρ_t [2]. A study done by the Department of Physics at Harvard University measured the total effective throughput of Pan-Starrs using a calibrated Silicon photodiode and a tunable laser. At even intervals of the wavelengths of the wideband filter, 0.5, 0.6, 0.7 and 0.8 μm, the study found that the optical transmittances for PS1 are approximately 0.67, 0.85, 0.99, and 0.95, respectively [22]. These values will be used as the values for the product $\eta\tau_o$. The typical exposure time, Δt, of a Pan-Starrs image will be about 30 seconds [11]. The furthest range, R, defining a NEO is 1.3 AUs, or approximately $1.9448 \times 10^{11} m$ [1]. A complete derivation of Eq. (7) is found in [16].

The expected number of photons incident on the aperture over the exposure time of the detector for objects making up the background radiation requires a different method than Eq. (7). The AB apparent magnitude system is a measure of the relative irradiance of celestial objects. Alpha Lyr (Vega) is the reference magnitude (zero magnitude) on the AB system. The number of photons received from the object is proportional to the irradiance of the object; therefore, if the expected number of photons from Vega is calculated, the AB system can be used as a measure of the relative number

19

of photons between two objects [23]. In the AB system, the magnitude of an object, M_s

is

$$M_s = -2.5 \ \log_{10}(F) - 48.585 , \tag{8}$$

where F is the flux, in $\frac{ergs}{cm^2}$. The relative difference in magnitude between two objects,

$M_s - M_N = M_x$ equates to a factor of 2.512^{M_x} decrease in irradiance or photons. Using

this, the relation between the number of expected photons received between an object of

interest and the reference Vega is

$$M_s - M_V = M_s ,$$

$$2.512^{M_s} = \frac{\overline{K}_V}{\overline{K}_s} ,$$

$$\overline{K}_s = \frac{\overline{K}_V}{2.512^{M_s}} , \tag{9}$$

where $M_V = 0$, the magnitude of Vega, $\overline{K}_V$ is the expected number of photons received

from Vega at the detector, $\overline{K}_s$ is the expected number of photons received from the

source, and M_s is the magnitude of the source, say a star, on the AB magnitude system

and can typically be found from a look-up table. Solving Eq. (9) requires $\overline{K}_V$, found by

$$\overline{K}_V = \frac{F \cdot B \cdot A \cdot \Delta t}{E} , \tag{10}$$

where:

- F is the flux in Joules per square meter,
- B is the bandwidth of the Pan-Starrs wideband filter used in NEO detection in Hz,

- A is the area of the aperture in square meters,
- Δt is the exposure time in seconds, and
- E is the energy per photon in Joules per photon.

To find the flux, set $M_s = M_V = 0$ and solve for F in Eq. (8), and then convert the units of the flux to equal the units of the flux in Eq. (10):

$$F = \left(3.6813 \times 10^{-20} \frac{ergs}{cm^2}\right)\left(\frac{10^{-7}J}{erg}\right)\left(\frac{10^4 cm^2}{m^2}\right),$$

$$= 3.6813 \times 10^{-23} \frac{J}{m^2}. \tag{11}$$

The energy per photon is wavelength dependent, and the wideband filter passes 500 nm to 800 nm wavelengths. A close approximation of the expected number of photons received will sum the number of photons received for each of the wavelengths 500 nm, 600 nm, 700 nm, and 800 nm. The calculation for each of the wavelengths will divide the bandwidth of the wideband filter into four equal bands: 500-575 nm, 575-650 nm, 650-725 nm, and 725-800 nm. At 500 nm, each photon has a frequency, f of roughly $6.0 \times 10^{14} Hz$. The energy in each photon at 500 nm, E, is

$$E = hf$$
$$= \left(6.626068 \times 10^{-34} J \cdot s\right)\left(6.0 \times 10^{14} Hz\right)$$
$$= 3.9756 \times 10^{-19} J$$

where h is Plank's constant. The bandwidth, B, used in Eq. (10) for this wavelength is:

$$B = \frac{c}{500nm} - \frac{c}{575nm}$$
$$= 7.82609 \times 10^{13} Hz,$$

where c is the speed of light. The number of expected photons from Vega in the band 500 to 575 nm, $\bar{K}_{V1}$ received by the 1.8m Pan-Starrs mirror in a 30 second exposure, using Eq. (10) is:

$$\bar{K}_{V1} = \frac{\left(3.6813\times10^{-23}\,\dfrac{J}{m^2}\right)\left(7.82609\times10^{13}\,Hz\right)\left(30s\right)\left(0.9m\right)^2\,\pi}{3.9756\times10^{-19}\,J\Big/photon}$$

$$= 5.53215\times10^{11}\,photons$$

Similar calculations for the remaining three wavelengths yields the number of expected photons from Vega in the band 575 to 650 nm, $K_{V2} = 5.1066\times10^{11}\,photons$, in the band 650 to 725 nm, $K_{V3} = 4.72506\times10^{11}\,photons$, and in the band 725 to 800 nm, $K_{V4} = 4.38756\times10^{11}\,photons$. The total number of expected photons received in a 30 second exposure using the wideband filter of Pan-Starrs is the sum of the number of photons from each wavelength:

$$\bar{K}_V = \bar{K}_{V1} + \bar{K}_{V2} + \bar{K}_{V3} + \bar{K}_{V4},$$

$$= 1.97513\times10^{12}\,photons. \qquad (12)$$

Now, given the magnitude of a celestial object, Eq. (9), and Eq. (12), it is possible to calculate the expected number of photons received by the detector of Pan-Starrs from any object. This will be used to model stars during simulations with varying brightness which contribute varying amounts of background radiation in the scene where a very dim NEO may be located.

Using $\bar{K}_N$ from Eq. (7), $\bar{K}_V$ from Eq. (12), and Eq. (9), it is possible to calculate the apparent magnitude of the NEO. By setting $\bar{K}_s = \bar{K}_N$ and $M_s = M_N$ in Eq. (9) and

solving for M_N by taking the natural logarithm of both sides, the apparent magnitude of

the NEO, M_N is

$$M_N = \frac{\ln(\bar{K}_V) - \ln(\bar{K}_N)}{\ln(2.512)}.$$ (13)

3.3 Likelihood Ratio Test

A LRT is a detection test that compares the ratio of two probabilities conditioned alternately on two hypotheses to a threshold. A complete derivation of the LRT can be found in [16]. The LRT is defined as

$$\Lambda = \frac{P(d(x,y) \forall (x,y) \in [1, M_d] | H_1)}{P(d(x,y) \forall (x,y) \in [1, M_d] | H_0)} \underset{H_0}{\overset{H_1}{\underset{<}{>}}} \eta.$$ (14)

Recall that M_d is the number of pixels in one dimension of the simulated square detector

plane. H_1 is the hypothesis that a NEO is present, and H_0 is the hypothesis that a NEO

is not present. $P(d(x,y) \forall (x,y) \in [1, M_d] | H_i)$ is the probability of the data at the (x,y) pixel

given hypothesis H_i, $i \in \{0,1\}$. The bounds on x and y will be assumed for the

remainder of the document and the notation will be shortened to $P[d(x,y)|H_i]$. In

practical applications, a Neyman-Pearson detection test in which the detection threshold

is set to a value that produces a desired false alarm rate should be used in NEO detection.

For purposes of comparing the performance of the current and proposed methods, a

Bayesian detection test is used in order to sweep through all possible values of thresholds

and generate a ROC curve.

As previously stated, the number of photons reflected from a NEO that are converted to photo-electrons by the detector of PS1 has a Poisson distribution with mean and variance equal to $\bar{K}_N$ from Eq. (7), similarly photons from background radiation are Poisson with mean and variance equal to $\bar{K}_S$ from Eq. (9). Given the properties of Poisson random variables, the composite image, or the sum of the photons from all objects in the scene is also Poisson. The current method of detection by Pan-Starrs without making simplifying approximations about the distributions of the photons does not lend itself to a LRT. Subtracting the master image, which is the deterministic mean of the sky image, from one exposure, which is Poisson distributed, results in a random variable whose mean and variance can be calculated, but whose mass function is no longer Poisson. One property of the Poisson random variable that simplifies this problem is that the Poisson random variable is well approximated as a Gaussian random variable with mean and variance equal to the parameter $\bar{K}$, under high illumination conditions. The difference between a Gaussian random variable and a deterministic variable is still Gaussian, with a shifted mean. This approximation makes a LRT much more feasible and its derivation follows [20].

$$\Lambda_G = \frac{P\left[d(x,y)|H_1\right]}{P\left[d(x,y)|H_0\right]} \overset{H_1}{\underset{H_0}{\overset{>}{<}}} \eta \tag{15}$$

where:

$$d\,|\,H_1 \sim Gaus\left\{\bar{K}_B + \left(\bar{K}_N + \bar{K}_S\right) * g, \sigma^2\right\}$$
$$d\,|\,H_0 \sim Gaus\left\{\bar{K}_B + \bar{K}_S * h, \sigma^2\right\}$$

- d is the data,
- H_1 is the hypothesis that a NEO is present in the scene,

24

- H_0 is the hypothesis that a NEO is not present in the scene,
- $\bar{K}_B$ is the expected number of photons received from background noise,
- $\bar{K}_S$ is the expected number of photons received from known objects in the image,
- $\bar{K}_N$ is the expected number of photons received from a NEO,
- g is the impulse response of the system,
- σ^2 is the variance (set equal for both hypotheses to reproduce Pan-Starrs detection scheme), and
- η is the threshold of detection.

The master image, I_M is

$$I_M = \bar{K}_B + \bar{K}_S * g , \tag{16}$$

and

$$P\big[d(x,y)|H_1\big] = \prod_x \prod_y \frac{1}{\sqrt{2\pi}\sigma} e^{\left\{-\frac{1}{2\sigma^2}\left[d(x,y)-\bar{K}_B-\left(\bar{K}_N+\bar{K}_S\right)*g\right]^2\right\}} .$$

Using properties of convolution,

$$P\big[d(x,y)|H_1\big] = \prod_x \prod_y \frac{1}{\sqrt{2\pi}\sigma} e^{\left\{-\frac{1}{2\sigma^2}\left[d(x,y)-I_M(x,y)-\bar{K}_N*g\right]^2\right\}} . \tag{17}$$

The objects from which photons are arriving can be viewed as a point source (a scaled Dirac delta function) due to the fact that the angular size of the objects, ignoring larger objects within the solar system, are smaller than one pixel in the detector plane; therefore, in general

$$\bar{K}_m * g = \bar{K}_m \sum_\alpha \sum_\beta \delta\big(\alpha_m - x - \alpha, \beta_m - y - \beta\big) g\big(\alpha, \beta\big),$$

$$= \bar{K}_m g\big(\alpha_m - x, \beta_m - y\big), \tag{18}$$

25

where (α_m, β_m) is the location of the point source with magnitude $\bar{K}_m$, the average number of photons received from object m. For the remainder of the document, photon source objects will be from stars located at (α_S, β_S) with an average number of received photons of $\bar{K}_S$, NEOs located at (α_N, β_N) with an average number of received photons of $\bar{K}_N$, and average background photons at each pixel, $\bar{K}_B$.

Now, Eq. (16) becomes

$$I_M(x, y) = \bar{K}_B + \bar{K}_S g(\alpha_S - x, \beta_S - y), \tag{19}$$

and Eq. (17) becomes

$$P\big[d(x, y) | H_1\big] = \prod_x \prod_y \frac{1}{\sqrt{2\pi}\sigma} e^{\left\{-\frac{1}{2\sigma^2}\left[d(x,y) - I_M(x,y) - \bar{K}_N g(\alpha_N - x, \beta_N - y)\right]^2\right\}}, \tag{20}$$

similarly,

$$P\big[d(x, y) | H_0\big] = \prod_x \prod_y \frac{1}{\sqrt{2\pi}\sigma} e^{\left\{-\frac{1}{2\sigma^2}\left[d(x,y) - I_M(x,y)\right]^2\right\}}. \tag{21}$$

Computing the LRT using Eq. (20) and Eq. (21), Eq. (15) becomes

$$\Lambda_G = \frac{P\big[d(x, y) | H_1\big]}{P\big[d(x, y) | H_0\big]} \overset{H_1}{\underset{H_0}{\gtrless}} \eta$$

$$= \frac{\displaystyle\prod_x \prod_y \frac{1}{\sqrt{2\pi}\sigma} e^{\left\{-\frac{1}{2\sigma^2}\left[d(x,y) - I_M(x,y) - \bar{K}_N g(\alpha_N - x, \beta_N - y)\right]^2\right\}}}{\displaystyle\prod_i \prod_j \frac{1}{\sqrt{2\pi}\sigma} e^{\left\{-\frac{1}{2\sigma^2}\left[d(i,j) - I_M(i,j)\right]^2\right\}}} \overset{H_1}{\underset{H_0}{\gtrless}} \eta. \tag{22}$$

It can be shown that:

$$\frac{\prod_{i=1}^{n} f(x_i)}{\prod_{j=1}^{n} g(y_j)} = \frac{f(x_1)f(x_2)\cdot\ldots\cdot f(x_n)}{g(y_1)g(y_2)\cdot\ldots\cdot g(y_n)} = \frac{f(x_1)}{g(y_1)}\cdot\frac{f(x_2)}{g(y_2)}\cdot\ldots\cdot\frac{f(x_n)}{g(y_n)} = \prod_{i=1}^{n}\frac{f(x_i)}{g(y_i)},$$

Eq. (22) simplifies to

$$\Lambda_G = \prod_x\prod_y \frac{e^{\left\{-\frac{1}{2\sigma^2}[d(x,y)-I_M(x,y)-\bar{K}_N g(\alpha_N-x,\beta_N-y)]^2\right\}}}{e^{\left\{-\frac{1}{2\sigma^2}[d(x,y)-I_M(x,y)]^2\right\}}} \underset{H_0}{\overset{H_1}{\underset{<}{\gtrless}}} \eta$$

$$\Lambda_G = \prod_x\prod_y e^{\left\{-\frac{1}{2\sigma^2}[d(x,y)-I_M(x,y)-\bar{K}_N g(\alpha_N-x,\beta_N-y)]^2+\frac{1}{2\sigma^2}[d(x,y)-I_M(x,y)]^2\right\}} \underset{H_0}{\overset{H_1}{\underset{<}{\gtrless}}} \eta .$$

Next, square the terms of the exponential, combine like terms and simplify:

$$\Lambda_G = \prod_x\prod_y e^{\frac{\bar{K}_N}{\sigma^2}\left\{-\frac{\bar{K}_N}{2}g^2(\alpha_N-x,\beta_N-y)+d(x,y)g(\alpha_N-x,\beta_N-y)-I_M(x,y)g(\alpha_N-x,\beta_N-y)\right\}} \underset{H_0}{\overset{H_1}{\underset{<}{\gtrless}}} \eta ,$$

$$\Lambda_G = e^{\sum_x\sum_y\frac{\bar{K}_N}{\sigma^2}\left\{-\frac{\bar{K}_N}{2}g^2(\alpha_N-x,\beta_N-y)+d(x,y)g(\alpha_N-x,\beta_N-y)-I_M(x,y)g(\alpha_N-x,\beta_N-y)\right\}} \underset{H_0}{\overset{H_1}{\underset{<}{\gtrless}}} \eta .$$

Finally, take the Natural Logarithm of both sides and simplify, noting that $\frac{\bar{K}_N}{\sigma^2} \geq 0$:

$$\ln\Lambda_G = \sum_x\sum_y d(x,y)g(\alpha_N-x,\beta_N-y)-\sum_x\sum_y I_M(x,y)g(\alpha_N-x,\beta_N-y) \underset{H_0}{\overset{H_1}{\underset{<}{\gtrless}}} \frac{\sigma^2\ln\eta}{\bar{K}_N}+\sum_x\sum_y\frac{\bar{K}_N}{2}g^2(\alpha_N-x,\beta_N-y),$$

where the right side of the equation is some constant, γ and (α_N,β_N) are the hypothesized coordinates of the NEO, and fall within some range $(\alpha,\beta)\in[1,M_d]$.

$$\ln\Lambda_G(\alpha,\beta) = \sum_x\sum_y d(x,y)g(\alpha-x,\beta-y)-\sum_x\sum_y I_M(x,y)g(\alpha-x,\beta-y) \underset{H_0}{\overset{H_1}{\underset{<}{\gtrless}}} \gamma ,$$

$$= \sum_x \sum_y \left[d(x,y) - I_M(x,y) \right] g(\alpha - x, \beta - y) \overset{H_1}{\underset{H_0}{\gtrless}} \gamma,$$

$$= (d - I_M) * g \overset{H_1}{\underset{H_0}{\gtrless}} \gamma. \tag{23}$$

Eq. (23), which precisely describes the Pan-Starrs method, shows that using peak detection on the convolution of the difference image with the PSF as a detection algorithm, has built into it the assumption that the photon data received is Gaussian and that the variance of the photon data is equal for both H_1 and H_0.

If a Poisson model is used for the noise in the imagery, the log-likelihood ratio test is:

$$\Lambda_P = \frac{P\left[d(x,y)\mid H_1\right]}{P\left[d(x,y)\mid H_0\right]} \overset{H_1}{\underset{H_0}{\gtrless}} \eta, \tag{24}$$

where,

$$d\mid H_1 \sim Pois\left\{\bar{K}_B + \left(\bar{K}_N + \bar{K}_S\right) * g\right\}$$
$$d\mid H_0 \sim Pois\left\{\bar{K}_B + \bar{K}_S * g\right\}$$

$$P\left[d(x,y)\mid H_1\right] = \prod_x \prod_y \frac{\left[\bar{K}_B + \left(\bar{K}_N + \bar{K}_S\right) * g\right]^{d(x,y)} e^{\left\{-\bar{K}_B - \left(\bar{K}_N + \bar{K}_S\right) * g\right\}}}{d(x,y)!}.$$

Using Eq. (16) and Eq. (18):

$$P\left[d(x,y)\mid H_1\right] = \prod_x \prod_y \frac{\left[I_M(x,y) + \bar{K}_N g\left(\alpha_N - x, \beta_N - y\right)\right]^{d(x,y)} e^{\left\{-I_M(x,y) - \bar{K}_N g(\alpha_N - x, \beta_N - y)\right\}}}{d(x,y)!}, \tag{25}$$

similarly,

28

$$P\left[d(x,y)\,|\,H_0\right]=\prod_x\prod_y\frac{\left[I_M(x,y)\right]^{d(x,y)}e^{\{-I_M(x,y)\}}}{d(x,y)!}\,. \tag{26}$$

Computing the LRT using Eq. (25) and Eq. (26), Eq. (24) becomes

$$\Lambda_P=\prod_x\prod_y\frac{\dfrac{\left[I_M(x,y)+\bar{K}_Ng(\alpha_N-x,\beta_N-y)\right]^{d(x,y)}e^{\{-I_M(x,y)-\bar{K}_Ng(\alpha_N-x,\beta_N-y)\}}}{d(x,y)!}}{\dfrac{\left[I_M(x,y)\right]^{d(x,y)}e^{\{-I_M(x,y)\}}}{d(x,y)!}}\underset{H_0}{\overset{H_1}{\gtrless}}\eta\,,$$

$$\Lambda_P=\left\{\prod_x\prod_y\left[\frac{I_M(x,y)+\bar{K}_Ng(\alpha_N-x,\beta_N-y)}{I_M(x,y)}\right]^{d(x,y)}\right\}e^{-\bar{K}_N\sum_x\sum_y g(\alpha_N-x,\beta_N-y)-\sum_x\sum_y I_M(x,y)+\sum_x\sum_y I_M(x,y)}\underset{H_0}{\overset{H_1}{\gtrless}}\eta$$

.

Take the natural logarithm of both sides and simplify,

$$\ln\Lambda_P=\sum_x\sum_y\frac{d(x,y)}{\bar{K}_N}\ln\left\{1+\frac{\bar{K}_Ng(\alpha_N-x,\beta_N-y)}{I_M(x,y)}\right\}\underset{H_0}{\overset{H_1}{\gtrless}}\frac{\ln\eta}{\bar{K}_N}+\sum_x\sum_y g(\alpha_N-x,\beta_N-y)\cdot$$

The threshold, η, for Bayesian detection where the prior probability of a NEO being present is equal and uniform costs are assumed, is set equal to one. It is assumed that the prior probability of a NEO being present or not is equal, which would be grossly inaccurate; however, the goal is to compare the performance with the use of ROC curves, which vary the threshold over all possible values. The number of photons received from a NEO, $\bar{K}_N$ is unknown. The simplifying assumption on the prior probability of the presence of a NEO, allows the term on the right side of the equation containing $\bar{K}_N$ to go to zero. It will be shown in the next section that $\bar{K}_N$, when estimated depends on the data received, and therefore should not be on the right side of the equation. Without any

29

usable data to formulate a value for η, the inaccurate assumption to set it to 1 is necessary. The remainder of the right side of the equation will be set to some constant, γ in order to sweep through all possible thresholds and create a ROC curve. As with the Gaussian LRT derivation, (α_N, β_N) are the hypothesized coordinates of the NEO, and falls within some range, $(\alpha, \beta) \in [1, M_d]$.

$$\ln \Lambda_P (\alpha, \beta) = \sum_x \sum_y \frac{d(x, y)}{\bar{K}_N} \ln \left\{ 1 + \frac{\bar{K}_N g(\alpha - x, \beta - y)}{I_M (x, y)} \right\} \underset{H_0}{\overset{H_1}{\underset{<}{\overset{>}{}}}} \gamma \qquad (27)$$

It should be noted that Eq. (27) does not estimate the location of a NEO, it merely detects the presence of a NEO in the image. Estimation theory can be applied to estimate (α_N, β_N), the simplest, but not necessarily the optimal estimate would be a peak detection on the two dimensional likelihood matrix, $\ln \Lambda_P (\alpha, \beta)$.

3.4   NEO Magnitude Estimation

The total number of photons received in an image, K is the summation of the number of photons received at each pixel, d

$$K = \sum_x \sum_y d(x, y). \qquad (28)$$

The summation of Poisson random variables is Poisson distributed with mean and variance equal to the sum of the means and variances of each component random variable [20]. The mean of K is the summation of the expected number of photons received by

30

each source, in this case the photons received by the NEO, $\bar{K}_N$, the photons received by

any background stars, $\bar{K}_S$, and the photons received by background radiation, $\bar{K}_B$

$$\bar{K} = \bar{K}_N + \bar{K}_S + \bar{K}_B M_d^2 , \tag{29}$$

where M_d is the number of pixels in one dimension of the square detector plane. Given

that the PSF is normalized, performing a summation of all of the pixels of the master

image using Eq. (19) yields,

$$\sum_x \sum_y I_M (x, y) = \sum_x \sum_y \left[\bar{K}_B + \bar{K}_S g (\alpha_S - x, \beta_S - y) \right],$$

$$= \bar{K}_B M_d^2 + \bar{K}_S . \tag{30}$$

A Generalized LRT (GLRT) is formed when an unknown parameter is replaced by the

maximum likelihood estimate for that parameter [24]. The maximum likelihood estimate

of $\bar{K}_N$, $\hat{\bar{K}}_N$ can be found by

$$\hat{\bar{K}}_N = \arg \max_{\bar{K}_N} \left\{ \ln P \left(K \mid \bar{K}_N \right) \right\},$$

$$= \arg \max_{\bar{K}_N} \left\{ \ln \left| \frac{\left(\bar{K}_N + \sum_x \sum_y I_M (x, y) \right)^K e^{\left(-\bar{K}_N - \sum_x \sum_y I_M (x, y) \right)}}{K!} \right| \right\},$$

$$= \arg \max_{\bar{K}_N} \left\{ K \ln \left(\bar{K}_N + \sum_x \sum_y I_M (x, y) \right) - \bar{K}_N - \sum_x \sum_y I_M (x, y) - K! \right\}.$$

31

The argmax can be found by setting the partial derivative of the log-likelihood with respect to $\bar{K}_N$ equal to zero,

$$0 = \frac{\partial}{\partial \bar{K}_N}\left\{ K \ln\left(\bar{K}_N + \sum_x \sum_y I_M(x,y)\right) - \bar{K}_N - \sum_x \sum_y I_M(x,y) - K! \right\},$$

$$= \frac{K}{\hat{\bar{K}}_N + \sum_x \sum_y I_M(x,y)} - 1,$$

$$\hat{\bar{K}}_N = K - \sum_x \sum_y I_M(x,y),$$

$$= \sum_x \sum_y d(x,y) - \sum_i \sum_j I_M(i,j). \tag{31}$$

Using this estimate in the implementation of the Poisson GLRT algorithm not only introduces additional randomness into the GLRT, but it is dependent on the master image. The effect of this estimate will vary with the magnitude of any background stars in the image. The mean of the estimate is

$$E\left[\hat{\bar{K}}_N\right] = \bar{K}_N \tag{32}$$

The variance of the estimate is

$$Var\left(\hat{\bar{K}}_N\right) = \bar{K}_N + \sum_x \sum_y I_M(x,y) \tag{33}$$

This shows that the estimator is unbiased and the variance of the estimate will increase with the increase in photon counts from the master image. Analytically, the signal to noise ratio (SNR) will be used to predict whether the Poisson-based GLRT or the Gaussian-based LRT will perform best. The SNR will be defined as

$$SNR = \frac{E\left[\Lambda\left(\alpha_N, \beta_N\right)\middle|H_1\right] - E\left[\Lambda\left(\alpha_N, \beta_N\right)\middle|H_0\right]}{\sqrt{Var\left(\Lambda\left(\alpha_N, \beta_N\right)\right)}} \tag{34}$$

This definition accounts for the magnitude of separation of the mean between the two hypotheses. This reveals the ability of the algorithm to distinguish the presence of a NEO as the LRT is compared to a threshold while also not making false positive detections. The further the value of the LRT given H_1 is from the value of the LRT given H_0, the more detectable the object is without false positives. The statistical fluctuation of the LRT is indicative of the ability of the noise to drive the LRT value above or below the threshold. This definition of SNR assumes symmetry conditions with the variance of the LRT. While the variance of the LRT given the two hypotheses is not equal, the variance given H_1 is treated as an upper bound on the unconditioned LRT and the variance of the LRT given H_0 is treated as a lower bound on the unconditioned LRT enabling the use of Eq. (34) as the definition of SNR. The SNR of the LRT as defined is a metric that reveals the ability of the algorithm to achieve a high probability of detection and a low probability of false alarm.

3.5   SNR Analysis

The following analysis compares whether the SNR of the Poisson GLRT is higher than the Gaussian-based LRT, the larger SNR will be indicative of the better performing algorithm. First, the elements of Eq. (34) are derived for the Poisson-based GLRT. Looking at the logarithmic element of Eq. (27), the first approximation of the Taylor Series expansion is

$$\ln\left\{1+\frac{\bar{K}_N g\left(\alpha_N - x, \beta_N - y\right)}{I_M\left(x, y\right)}\right\} \approx \frac{\bar{K}_N g\left(\alpha_N - x, \beta_N - y\right)}{I_M\left(x, y\right)} \tag{35}$$

for
$$-1 < \frac{\bar{K}_N g\left(\alpha_N - x, \beta_N - y\right)}{I_M\left(x, y\right)} < 1.$$

A photon count of less than zero does not make physical sense; therefore, this approximation holds when

$$\bar{K}_N < \frac{I_M\left(x, y\right)}{g\left(\alpha_N - x, \beta_N - y\right)}.$$

Using the simulated PSF for Pan-Starrs and ranging the magnitudes for the background stars from the dimmest measureable star to the brightest star, the required value for $\bar{K}_N$ for this approximation to hold, regardless of the magnitude of the background image was found to be

$$\bar{K}_N < 15,000 \text{ photons}.$$

Eq. (33) shows that the variance of the maximum likelihood estimate for $\bar{K}_N$ may cause this restriction to be exceeded when the background image contains a large number of photons. When this scenario is encountered, the following SNR analysis no longer accurately predicts the performance of the LRT.

$$\Lambda_P\left(\alpha, \beta\right) = \sum_x \sum_y \frac{d\left(x, y\right)}{\hat{\bar{K}}_N} \ln\left[1 + \frac{\hat{\bar{K}}_N g\left(\alpha - x, \beta - y\right)}{I_M\left(x, y\right)}\right] \approx \sum_x \sum_y \frac{d\left(x, y\right)\hat{\bar{K}}_N g\left(\alpha - x, \beta - y\right)}{\hat{\bar{K}}_N I_M\left(x, y\right)}$$

The expected value of the Poisson-based LRT given H_1 is:

$$E\left[\Lambda_P\left(\alpha, \beta\right) \middle| H_1\right] \approx E\left[\sum_x \sum_y \frac{d\left(x, y\right) g\left(\alpha - x, \beta - y\right)}{I_M\left(x, y\right)}\right],$$

$$\approx \sum_x \sum_y \frac{E\big[d(x,y)\big]g(\alpha-x,\beta-y)}{I_M(x,y)},$$

$$\approx \sum_x \sum_y \frac{\big(K_N g(\alpha_N-x,\beta_N-y)g(\alpha-x,\beta-y)+I_M(x,y)g(\alpha-x,\beta-y)\big)}{I_M(x,y)},$$

$$\approx 1 + \sum_x \sum_y \frac{K_N g^2(\alpha_N-x,\beta_N-y)}{I_M(x,y)}. \tag{36}$$

The expected value of the Poisson-based LRT given H_0 is:

$$E\big[\Lambda_P(\alpha,\beta)\big|H_0\big] \approx \sum_x \sum_y \frac{E\big[d(x,y)\big]g(\alpha-x,\beta-y)}{I_M(x,y)},$$

$$\approx \sum_x \sum_y \frac{I_M(x,y)g(\alpha-x,\beta-y)}{I_M(x,y)} = 1. \tag{37}$$

The variance of the Poisson-based LRT given H_1 is:

$$Var\big(\Lambda_P(\alpha,\beta)\big|H_1\big) \approx E\left[\left(\sum_x \sum_y \frac{d(x,y)g(\alpha-x,\beta-y)}{I_M(x,y)}\right)^2\right],$$

$$-E^2\left[\sum_x \sum_y \frac{d(x,y)g(\alpha-x,\beta-y)}{I_M(x,y)}\right]$$

$$\approx \sum_{x_1}\sum_{y_1}\sum_{x_2}\sum_{y_2} \frac{E\big[d(x_1,y_1)\big]E\big[d(x_2,y_2)\big]g(\alpha-x_1,\beta-y_1)g(\alpha-x_2,\beta-y_2)}{I_M(x_1,y_1)I_M(x_2,y_2)}$$

$$-\sum_{x_1}\sum_{y_1}\frac{\big(E\big[d(x_1,y_1)\big]\big)^2 g^2(\alpha-x_1,\beta-y_1)}{I_M^2(x_1,y_1)}$$

$$+\sum_x \sum_y \frac{\Big(E\big[d(x,y)\big]+\big(E\big[d(x_1,y_1)\big]\big)^2\Big)g^2(\alpha-x,\beta-y)}{I_M^2(x,y)},$$

$$-\left(1+\sum_x \sum_y \frac{K_N g^2(\alpha_N-x,\beta_N-y)}{I_M(x,y)}\right)^2$$

$$\approx \sum_{x_1}\sum_{y_1}\sum_{x_2}\sum_{y_2}\left(\frac{E\left[d\left(x_1,y_1\right)\right]g\left(\alpha-x_1,\beta-y_1\right)}{I_M\left(x_1,y_1\right)}\right)\left(\frac{E\left[d\left(x_2,y_2\right)\right]g\left(\alpha-x_2,\beta-y_2\right)}{I_M\left(x_2,y_2\right)}\right)$$

$$-\cancel{\sum_{x_1}\sum_{y_1}\frac{\left(E\left[d\left(x_1,y_1\right)\right]\right)^2 g^2\left(\alpha-x_1,\beta-y_1\right)}{I_M^2\left(x_1,y_1\right)}}$$

,

$$+\sum_{x}\sum_{y}\frac{\left(E\left[d\left(x,y\right)\right]g^2\left(\alpha-x,\beta-y\right)\right)}{I_M^2\left(x,y\right)}+\cancel{\frac{\left(E\left[d\left(x_1,y_1\right)\right]\right)^2 g^2\left(\alpha-x,\beta-y\right)}{I_M^2\left(x,y\right)}}$$

$$-\left(1+\sum_{x}\sum_{y}\frac{K_N g^2\left(\alpha_N-x,\beta_N-y\right)}{K_S h\left(x-\alpha_S,y-\beta_S\right)+K_B}\right)^2$$

$$\approx \left[1+\cancel{\sum_{x_1}\sum_{y_1}\frac{K_N g\left(\alpha_N-x_1,\beta_N-y_1\right)g\left(\alpha-x_1,\beta-y_1\right)}{I_M\left(x_1,y_1\right)}}\right]^2$$

$$+\sum_{x}\sum_{y}\frac{\left(\left[K_N g\left(\alpha_N-x,\beta_N-y\right)g^2\left(\alpha-x,\beta-y\right)\right]\right)}{I_M^2\left(x,y\right)}+\frac{g^2\left(\alpha-x,\beta-y\right)}{I_M\left(x,y\right)},$$

$$-\left(1+\cancel{\sum_{x}\sum_{y}\frac{K_N g^2\left(\alpha_N-x,\beta_N-y\right)}{I_M\left(x,y\right)}}\right)^2$$

$$Var\left(\Lambda_P\left(\alpha_N,\beta_N\right)\middle|H_1\right)\approx\sum_{x}\sum_{y}\frac{K_N g^3\left(\alpha_N-x,\beta_N-y\right)}{I_M^2\left(x,y\right)}+\sum_{x}\sum_{y}\frac{g^2\left(\alpha_N-x,\beta_N-y\right)}{I_M\left(x,y\right)}. \tag{38}$$

The variance of the Poisson-based GLRT given H_0 is:

$$Var\left(\Lambda_P\left(\alpha,\beta\right)\middle|H_0\right)\approx\sum_{x_1}\sum_{y_1}\sum_{x_2}\sum_{y_2}\left(\frac{E\left[d\left(x_1,y_1\right)\right]g\left(\alpha-x_1,\beta-y_1\right)}{I_M\left(x_1,y_1\right)}\right)\left(\frac{E\left[d\left(x_2,y_2\right)\right]g\left(\alpha-x_2,\beta-y_2\right)}{I_M\left(x_2,y_2\right)}\right),$$

$$+\sum_{x}\sum_{y}\frac{\left(E\left[d\left(x,y\right)\right]g^2\left(\alpha-x,\beta-y\right)\right)}{I_M^2\left(x,y\right)}-1$$

$$\approx \cancel{\sum_{x_1}\sum_{y_1}\sum_{x_2}\sum_{y_2}\left(\frac{I_M\left(x_1,y_1\right)g\left(\alpha-x_1,\beta-y_1\right)}{I_M\left(x_1,y_1\right)}\right)\left(\frac{I_M\left(x_2,y_2\right)g\left(\alpha-x_2,\beta-y_2\right)}{I_M\left(x_2,y_2\right)}\right)},$$

$$+\sum_{x}\sum_{y}\frac{I_M\left(x,y\right)g^2\left(\alpha-x,\beta-y\right)}{I_M^2\left(x,y\right)}\cancel{-1}$$

$$Var\left(\Lambda_P\left(\alpha_N,\beta_N\right)\middle|H_0\right)\approx\sum_{x}\sum_{y}\frac{g^2\left(\alpha_N-x,\beta_N-y\right)}{I_M\left(x,y\right)}. \tag{39}$$

The difference between Eq. (38) and Eq. (39) is the term

$$\sum_x \sum_y \frac{K_N g^3 \left(\alpha_N - x, \beta_N - y\right)}{I_M^2 \left(x, y\right)},$$

which is much less than Eq. (39) for small diameter NEOs. The SNR as defined by Eq. (34) is bounded by

$$\frac{\sum_x \sum_y \frac{K_N g^2 \left(\alpha_N - x, \beta_N - y\right)}{I_M \left(x, y\right)}}{\sqrt{\sum_x \sum_y \frac{K_N g^3 \left(\alpha_N - x, \beta_N - y\right)}{I_M^2 \left(x, y\right)} + \sum_x \sum_y \frac{g^2 \left(\alpha_N - x, \beta_N - y\right)}{I_M \left(x, y\right)}}} \leq SNR_{\Lambda_P} \leq \frac{\sum_x \sum_y \frac{K_N g^2 \left(\alpha_N - x, \beta_N - y\right)}{I_M \left(x, y\right)}}{\sqrt{\sum_x \sum_y \frac{g^2 \left(\alpha_N - x, \beta_N - y\right)}{I_M \left(x, y\right)}}}, \quad (40)$$

where the bounds are approximately equal for small NEOs. Eq. (40) is independent of the maximum likelihood estimate, $\hat{\hat{K}}_N$, which suggests that the value used for $\hat{\hat{K}}_N$ does not affect the performance of the LRT. Recall that Eq. (40) was derived with the approximation in Eq. (35), and that the conditions under which this approximation holds can be exceeded if the value used for $\hat{\hat{K}}_N$ is large. When the variance of this estimate causes the restrictions on the approximation in Eq. (35) to be increasingly exceeded, the net effect of using this estimate is an increased variance of the value of the GLRT. The increased variance of the GLRT is due to one of the uses of the estimate being inside a logarithmic term and the other being in the denominator outside the logarithmic term. The increased variance of the GLRT will cause a decrease in the expected SNR. Given that the SNR does not depend on the value for $\hat{\hat{K}}_N$ unless it is large, and the variance of $\hat{\hat{K}}_N$ can be very large depending on the background master image, an easy way to eliminate the possibility of $\hat{\hat{K}}_N$ being inaccurately large is to set it equal to a small constant rather than its maximum likelihood estimate. Eq. (40) predicts this approach

37

will yield the best performance for the Poisson LRT under all environmental scenarios; therefore, the Poisson-based LRT as opposed to the GLRT will be used with the unknown parameter $\hat{K}_N$ set equal to one. Simulations will be used to verify this qualitative analysis.

A similar derivation produces the SNR for the Gaussian-based Pan-Starrs method. The expected value of the Gaussian-based LRT given H_1 is:

$$E\left[\Lambda_G(\alpha,\beta)\middle|H_1\right]=\sum_x\sum_y\left\{E\left[d(x,y)\right]g(\alpha-x,\beta-y)-I_M(x,y)g(\alpha-x,\beta-y)\right\},$$

$$=\sum_x\sum_y\left\{\begin{array}{l}K_Ng(\alpha_N-x,\beta_N-y)g(\alpha-x,\beta-y)\\ \overline{+I_M(x,y)g(\alpha-x,\beta-y)}\\ \overline{-I_M(x,y)g(\alpha-x,\beta-y)}\end{array}\right\},$$

$$E\left[\Lambda_G(\alpha_N,\beta_N)\middle|H_1\right]=\sum_x\sum_y K_Ng^2(\alpha_N-x,\beta_N-y). \tag{41}$$

The expected value of the Gaussian-based LRT given H_0 is:

$$E\left[\Lambda_G(\alpha,\beta)\middle|H_0\right]=\sum_x\sum_y\left\{E\left[d(x,y)\right]g(\alpha-x,\beta-y)-I_M(x,y)g(\alpha-x,\beta-y)\right\},$$

$$=\sum_x\sum_y\left(\overline{I_M(x,y)g(\alpha-x,\beta-y)}\right)\overline{-I_M(x,y)g(\alpha-x,\beta-y)},$$

$$E\left[\Lambda_G(\alpha,\beta)\middle|H_0\right]=0. \tag{42}$$

The variance of the Gaussian-based LRT given H_1 is:

$$Var\left(\Lambda_G(\alpha,\beta)\middle|H_1\right)=E\left[\left(\Lambda_G(\alpha,\beta)\middle|H_1\right)^2\right]-E^2\left[\Lambda_G(\alpha,\beta)\middle|H_1\right],$$

38

$$= E\left[\left(\sum_x \sum_y \left(d(x,y) - I_M(x,y)\right) g(\alpha - x, \beta - y)\right)^2\right]$$

$$- \left[\sum_x \sum_y K_N g^2(\alpha_N - x, \beta_N - y)\right]^2 ,$$

$$= E\left[\sum_{x_1} \sum_{y_1} \sum_{x_2} \sum_{y_2} \left\{ \begin{array}{l} \left[d(x_1,y_1) - I_M(x_1,y_1)\right] \\ \cdot \left[d(x_2,y_2) - I_M(x_2,y_2)\right] \\ \cdot g(\alpha - x_1, \beta - y_1) g(\alpha - x_2, \beta - y_2) \end{array} \right\} \right]$$

$$- E\left[\sum_{x_1} \sum_{y_1} \sum_{x_2} \sum_{y_2} \left\{ \begin{array}{l} \left[d(x_1,y_1) - I_M(x_1,y_1)\right] \\ \cdot \left[d(x_2,y_2) - I_M(x_2,y_2)\right] \\ \cdot g(\alpha - x_1, \beta - y_1) g(\alpha - x_2, \beta - y_2) \end{array} \right\} \right]$$

$$\cdot \delta(x_1 - x_2, y_1 - y_2)$$

$$+ E\left[\sum_x \sum_y \left[d(x,y) - I_M(x,y)\right]^2 g^2(\alpha - x, \beta - y)\right]$$

$$- \left[\sum_x \sum_y K_N g^2(\alpha_N - x, \beta_N - y)\right]^2 ,$$

$$= \sum_{x_1} \sum_{y_1} \sum_{x_2} \sum_{y_2} \left[\begin{array}{l} \left\{E\left[d(x_1,y_1)\right] - I_M(x_1,y_1)\right\} \\ \cdot \left\{E\left[d(x_2,y_2)\right] - I_M(x_2,y_2)\right\} \\ \cdot g(\alpha - x_1, \beta - y_1) g(\alpha - x_2, \beta - y_2) \end{array} \right]$$

$$- \sum_{x_1} \sum_{y_1} \left\{E\left[d(x_1,y_1)\right] - I_M(x_1,y_1)\right\}^2 g^2(\alpha - x_1, \beta - y_1)$$

$$+ \sum_x \sum_y \left[\left\{ \begin{array}{l} E\left[d(x_1,y_1)\right] + E^2\left[d(x,y)\right] \\ -2E\left[d(x_1,y_1)\right] I_M(x,y) \\ + I_M^2(x,y) \end{array} \right\} \cdot g^2(\alpha - x, \beta - y) \right]$$

$$- \left[\sum_x \sum_y K_N g^2(\alpha_N - x, \beta_N - y)\right]^2 ,$$

39

$$= \sum_x \sum_y K_N g\left(\alpha_N - x, \beta_N - y\right) g^2\left(\alpha - x, \beta - y\right)$$
$$+ \sum_x \sum_y I_M\left(x, y\right) g^2\left(\alpha - x, \beta - y\right) \qquad ,$$

$$Var\left(\Lambda_G\left(\alpha_N, \beta_N\right) \big| H_1\right) = \sum_x \sum_y K_N g^3\left(\alpha_N - x, \beta_N - y\right)$$
$$+ \sum_x \sum_y I_M\left(x, y\right) g^2\left(\alpha_N - x, \beta_N - y\right) . \qquad (43)$$

The variance of the Gaussian-based LRT given H_0 after going through similar steps as in

the H_1 case is:

$$Var\left(\Lambda_G\left(\alpha, \beta\right) \big| H_0\right) = \sum_x \sum_y \left[E\left[d\left(x_1, y_1\right)\right] g^2\left(\alpha - x, \beta - y\right) \right],$$

$$Var\left(\Lambda_G\left(\alpha_N, \beta_N\right) \big| H_0\right) = \sum_x \sum_y I_M\left(x, y\right) g^2\left(\alpha_N - x, \beta_N - y\right). \qquad (44)$$

As with the variance of the Poisson-based LRT given the two hypotheses, the variance of

the Gaussian-based LRT given both hypotheses are approximately equal for small NEOs.

The SNR of the Gaussian-based LRT is bounded by

$$\frac{\sum_x \sum_y K_N g^2\left(\alpha_N - x, \beta_N - y\right)}{\sqrt{\sum_x \sum_y K_N g^3\left(\alpha_N - x, \beta_N - y\right) + \sum_x \sum_y I_M\left(x, y\right) g^2\left(\alpha_N - x, \beta_N - y\right)}} \leq SNR_{\Lambda_G} \leq \frac{\sum_x \sum_y K_N g^2\left(\alpha_N - x, \beta_N - y\right)}{\sqrt{\sum_x \sum_y I_M\left(x, y\right) g^2\left(\alpha_N - x, \beta_N - y\right)}}. \qquad (45)$$

Inspection of Eq. (40) and Eq. (45) indicates that the two algorithms should have close to

the same level of performance if the background master image is flat and small, meaning

that no background stars are in the image. This allows the master image term to be pulled

out of the summation and distributed through the denominator, which results in the same

expression for SNR whether Gaussian or Poisson distributions are used for photon

statistics. Both expressions of the bounds on the SNRs are completely characterized by

three parameters: the number of photons received from the NEO, the background master

image, and the PSF. The next section will introduce models used to simulate these parameters for numerical evaluation of the SNR expressions.

3.6   Monte Carlo Simulations

Simulations developed in Matlab® simulation software from Mathworks® will be used to verify the feasibility of the proposed Poisson-based LRT compared to the Gaussian-based LRT. The Matlab® code is located in the Appendix and is well commented to provide a functional description. The simulation uses the most detailed and accurate specifications available to build a model of the optical system, while making appropriate assumptions where necessary.

The code first creates the total impulse response, to include a model of PS1 and the average effects of the atmosphere. The code then generates two sets of data, one with a simulated NEO present and one without a simulated NEO present using Poisson statistics, and finally it calculates the LRT based on Gaussian assumptions as well as with Poisson. The impulse response is used to create simulated images by convolving it with a two dimensional Dirac delta function scaled by the expected number of photons for the object being represented. A master image is created in this way, but simulated data is created by feeding the average image into a Poisson noise generator. One thousand trials were run to create ROC curves for each of the two algorithms based on images of a 140 meter diameter NEO separated from a star by 28.21 arc-seconds. The angular separation of 28.21 arc-seconds equates to a 70 pixel on the diagonal separation in the modeled detector plain, given that PS1 has an angular resolution of 0.285 arc-seconds [11]. Different ROC curves were generated for star magnitudes ranging from 0, the relative

brightness of Vega to 25, approximately 2.5 times dimmer than a 140 meter diameter NEO at 1.3 AU from Earth. A simple comparison between curves can provide a metric of the effectiveness of that algorithm. The algorithm with a ROC curve with more area under the curve is generally a better performing algorithm.

Simulations also include varying other environmental situations besides the size of the NEO. The magnitude of background stars in the image is varied, as well as the angular separation between a NEO and a background star in the image. Additionally, ten thousand trials were run to calculate the probability of false alarm in these environments. The increase in the number of trials for false alarm rates provides more precision in calculating the false alarm rate. Limits in computing power prevent Monte Carlo simulations as a method to calculate a threshold that would yield extremely small false alarm rates, but simulations were used to calculate as precise a rate as possible with the ten thousand trials. False alarm rates smaller than those calculated with Monte Carlo simulations can be estimated by assuming the value of the LRT is Gaussian by using the Central Limit Theorem [20]. Any false alarm rate may then be estimated by simply estimating the mean and variance of the LRT. Choosing a specific false alarm rate, these three plots will be generated: the probability of detection versus angular separation between the NEO and a background star; the probability of detection versus the magnitude difference between the NEO and a background star, while the magnitude of the NEO is fixed; and the probability of detection versus the magnitude of the NEO while the magnitude of the background star is fixed.

3.7   System Model

If the telescope is assumed to be a linear, space-invariant system, all that is needed to model the telescope is its impulse response. The total impulse response is what is imaged when the system is interrogated with a point source. The system includes the atmosphere and the telescope. The total impulse response is the inverse Fourier transform of the product of the average atmospheric transfer function with the optical transfer function of the telescope, given by

$$g_{tot}(u,v) = F^{-1}\{G_{atm}(f_x, f_y)G_{opt}(f_x, f_y)\}. \qquad (46)$$

The first thing to consider when building the system model is proper spatial sampling for the detector plane, the aperture plane, and the atmosphere. If not sampled properly, aliasing will cause inaccurate results [16]. The simplest spatial sampling to determine is in the detector plane due to the fact that the spatial sampling of the PS1 in the detector plane is the size of the actual pixels of the CCD array of PS1, $\Delta_d = 10\mu m$ [11].

The spatial sampling in the aperture is slightly more difficult to arrive at. Nyquist sampling theorem requires a minimum of two samples per period, implying that the phase change in the aperture plane must be less than π. The field at the aperture, f_a, due to a point source a distance z away from the aperture is defined by

$$f_a(x,y,t) = \frac{ze^{j2\pi v[t - R_1(x,y)/c]}}{j\lambda R_1^2(x,y)}, \qquad (47)$$

43

where x and y are points measured from the center of the aperture. R_1 is the range from the point source to the aperture as a function of the location in the aperture, and is described by the distance equation

$$R_1(x, y) = \sqrt{(x\Delta_a)^2 + (y\Delta_a)^2 + z^2} .$$

(48)

The spatial sampling of the aperture, Δ_a is

$$\Delta_a = \frac{D}{M_a} ,$$

D is the diameter of the aperture, M_a is the number of samples in the simulated aperture plane. The binomial approximation of Eq. (48) is

$$R_1(x, y) \approx z \left[1 + \frac{(x\Delta_a)^2 + (y\Delta_a)^2}{2z^2} - \frac{\left((x\Delta_a)^2 + (y\Delta_a)^2\right)^2}{8z^4} + \cdots \right]$$

(49)

If all of the optics of PS1 are treated as a thin lens, the phase effects of the field through the optics of the telescope can be modeled at the aperture with a lens phase screen

$$t_{lens}(x, y) = e^{-j\frac{\pi\left((x\Delta_a)^2 + (y\Delta_a)^2\right)}{\lambda f}}$$

(50)

The phase of the lens phase screen cancels the quadratic term in Eq. (49), leaving the third term as the largest contributor to phase change at the aperture. The phase change of the aperture is described by

$$\Delta\varphi = \frac{\pi\left[\left(\frac{D}{2}\right)^4 - \left(\frac{D}{2} - \Delta_a\right)^4\right]}{4\lambda f^3}$$

(51)

which must be less than π to satisfy Nyquist sampling. The only element that is variable is $\Delta_a = \dfrac{D}{M_a}$, specifically M_a must be large enough to satisfy the phase requirement.

$$\Delta\varphi = \frac{\pi\left[\left(\dfrac{D}{2}\right)^4 - \left(\dfrac{D}{2} - \dfrac{D}{M_a}\right)^4\right]}{4\lambda f^3} \leq \pi$$

$$\frac{D^4}{4\lambda f^3}\left[\frac{1}{16} - \left(\frac{(M_a - 2)}{2M_a}\right)^4\right] \leq 1$$

$$\frac{D^4}{4\lambda f^3}\left[\frac{1}{16} - \frac{1}{16}\left(1 - \frac{2}{M_a}\right)^4\right] \leq 1$$

$$\frac{D^4}{64\lambda f^3}\left(1 - \frac{2}{M_a}\right)^4 \geq \frac{D^4}{64\lambda f^3} - 1$$

$$\left(1 - \frac{2}{M_a}\right)^4 \geq 1 - \frac{64\lambda f^3}{D^4}$$

$$M_a \geq \frac{2}{\left(1 - \sqrt[4]{1 - \dfrac{64\lambda f^3}{D^4}}\right)}$$

Using 500 nm for λ because the largest phase difference will occur with the smallest wavelength, 8 m for the focal length f, and 1.8 m for the diameter D, $M_a \geq 5123$ was found to ensure adequate sampling across the entire aperture [16].

The spatial sampling of the atmosphere requires a brief description of the atmospheric model. The largest contributor to phase error due to a turbulent atmosphere is tilt. Tilt can be modeled as a zero mean Gaussian random variable, which is correlated over a finite amount of time. Tilt across a small sample of time is highly correlated, but

samples taken over longer periods of time become more and more uncorrelated, until there is zero correlation between samples. The exposure time of one image taken by PS1 is typically 30 seconds. Over a 30 second period, the atmosphere at the start of the sample time is uncorrelated with the atmosphere at the end of the sample time, and the effect of tilt averages to zero. This allows the effect of tilt to be ignored in this model. Other aberrations caused by a turbulent atmosphere can be modeled by an average transfer function. The average transfer function for a long exposure is given by [25]

$$G_{atm}\left(f_x, f_y\right) = e^{-3.44\left(\frac{\lambda f \Delta_f \sqrt{f_X^2 + f_Y^2}}{r_0}\right)^{5/3}}$$ (52)

The frequency sampling of the atmosphere is

$$\Delta_f = \frac{1}{M_d \Delta_d}$$

where M_d is the number of pixels in one dimension of the simulated square detector plane and was chosen to be 100 pixels. The size of the image of a 140 meter wide object at 1.3 AUs with a focal length of 8 meters on the detector can be found using simple trigonometry and is approximately 5.6 μm, or just over half of a pixel; therefore, the complete image of the NEO will fit well within 100 pixels. The spatial sampling of the atmosphere,

$$\Delta_{atm} = \lambda f \Delta_f = \frac{\lambda f}{M_d \Delta_d}$$ (53)

ensures that Eq. (52) has the same number of samples in the frequency spectrum as the transfer function of the telescope [16].

Now that the proper sampling, Δ_{atm}, Δ_a, and Δ_d have been determined for the model, and the average transfer function for the atmosphere has been developed, the final step in obtaining the total impulse response from Eq. (46) is to develop the transfer function of the telescope. The transfer function of the telescope is the Fourier transform of the PSF, or the impulse response of the telescope. This is determined by propagating the field at the aperture due to a point source, through the optics of PS1. First a circular array that represents the aperture must be created. The field at the aperture can be modeled as a uniform plane wave. This is an appropriate approximation to a spherical wave (point source) propagated from a long distance [26]. If the field at the aperture is a uniform plane wave, then the aperture may be modeled as a binary screen, 1 inside the aperture and 0 outside. The lens phase screen, Eq. (50), is then multiplied to the field at the aperture to create the field $f_l(x_m, y_n)$, which is then propagated to the detector plane, located in the focal plane of the telescope system. The Rayleigh-Sommerfeld diffraction integral, propagates the field $f_l(x_m, y_n)$ a distance f, and the resulting field at the detector, $f_d(u,v,t)$ is

$$f_d(u,v,t) = \sum_{m=1}^{M_a} \sum_{n=1}^{M_a} \frac{f_l(x_m, y_n) f e^{j\frac{2\pi}{\lambda}\left[t - R_2(x_m, y_n, u, v)\right]}}{j\lambda R_2^{\,2}(x_m, y_n, u, v)}, \qquad (54)$$

in which R_2 is the distance between every pixel in the aperture plane and every pixel in the detector plane:

$$R_2(x_m, y_n, u, v) = \sqrt{\left(x_m \Delta_a - u\Delta_d\right)^2 + \left(y_n \Delta_a - v\Delta_d\right)^2 + f^2} \qquad (55)$$

The squared magnitude of Eq. (54) is the PSF of the telescope, so [26]

$$G_{opt}\left(f_X,f_Y\right)=F\left\{\left|f_d\left(u\Delta_d,v\Delta_d,t\right)\right|^2\right\}. \tag{56}$$

Now Eq. (46) is used to find the total impulse response of the system which completely characterizes the system for an arbitrary input. The output image due to the incidence of any input can be modeled as the convolution of the input with the impulse response [26].

3.8 Measured Data

Hardware with the capabilities of PS1 is not available to test the proposed hypothesis on actual image data; instead a relative test environment is developed to test the difference in the performance of the two LRT algorithms. Having a smaller telescope that is not capable to detecting NEOs, a brighter object is used and the integration time of the telescope will be adjusted to make the object difficult to detect. Polaris is chosen because its relative fixed location in the sky provides time to collect a large number of images without having to readjust the hardware or to register the images. Also, using a bright object that is detectable with the naked eye provides a known truth for hypothesis testing. Reducing the integration time of the CCD device on the telescope reduces the detectability of even a bright object. The integration time will be set to such a level that detection is difficult and a statistically significant number of images will be collected, ideally a minimum of one thousand images. These images will be averaged together to verify that Polaris is detected in the averaged data. Each image will be fed into each algorithm and ROC curves will be generated and compared as was done in simulations.

Background noise images from a location in the image that does not have an object will be used as the image data for H_0.

The CCD in the telescope has a gain factor that converts the photon count to a digital count that is not Poisson. To properly implement the proposed algorithm, the digital counts must be converted back into photon counts. For this conversion, the gain factor of the CCD is required. Consider the following.

$$d = \phi I$$

where

- d is the digital count data,
- ϕ is the CCD gain factor, and
- I is the Poisson distributed photon count.

The expected value of the digital count is

$$E[d] = \phi E[I], \tag{57}$$

and the variance of the digital count is

$$Var(d) = \phi^2 \left(E[I^2] - E^2[I] \right)$$

$$Var(d) = \phi^2 Var(I) = \phi^2 E[I]. \tag{58}$$

The ratio of (58) to (57) results in an expression for the gain factor,

$$\frac{Var(d)}{E[d]} = \phi.$$

Both the variance and the expected value of the digital count data can be adequately estimated with a reasonable number of sample images. Converting the digital count back into photon count will, however induce some quantization noise [24].

3.9   Summary

This chapter described the theory supporting the basis for the Poisson-based LRT, as well as the methodology for comparing the performance of the Poisson-based LRT to the performance of the Gaussian-based LRT. The methodology addresses the comparison of the two algorithms in three ways. First, analysis is performed on the expected SNR of each LRT. The LRT which has a larger SNR should be indicative of the better performing algorithm. Secondly, Monte Carlo simulations are performed based on complex models of hardware and environmental characteristics, in which the two algorithms are compared in several different scenarios. Lastly, measured data is taken in a relative test environment and the performance of each algorithm with the measured data is compared using ROC curves. The results of these methods are presented in the next chapter.

4   Analysis and Results

4.1   Chapter Overview

This chapter presents the results of the three approaches described in Chapter 3 to comparing the Gaussian-based LRT to the Poisson-based LRT. The first of these results is a numerical analysis of the SNR of each algorithm based on either actual parameters or modeled parameters. The second set of results is simulated data based on models of the hardware and environmental characteristics. The third set of results is measured data taken in a relative test environment.

4.2   Analytic Results

The SNR analysis requires a model for the PSF, a model for the expected number of photons received from a NEO and a model for the master image. The PSF was modeled with a seeing parameter of 8 cm as described in the previous chapter, and details of that model are discussed in the next section addressing simulated results.   The expected number of photons received by the detector of PS1 from a NEO of a desired diameter at a distance of 1.3 AU is calculated using Eq. (7) from Chapter 3.2. The master image is generated by convolving point sources of a desired magnitude with the modeled PSF and adding the average background photons.

The upper and lower bound on the SNR from Eq. (40) and Eq. (45) were calculated using modeled inputs for various master images and varied NEO sizes. The following graphs are a demonstrative subset of the results for the varied parameters. They display the SNR versus the apparent magnitude of a background star for different angular separations between the modeled NEO and star.   In Figure 7 the modeled
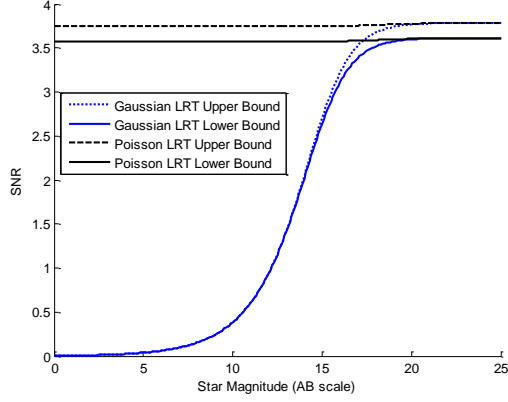
Figure 7. SNR of 140 m NEO vs. Star Mag;
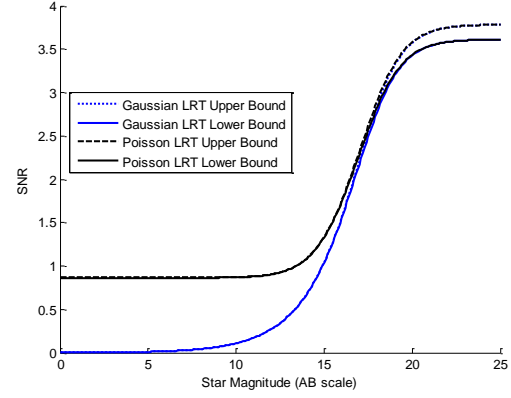
28.2 arc-sec Angular Separation

Figure 8. SNR of 140 m NEO vs. Star Mag;

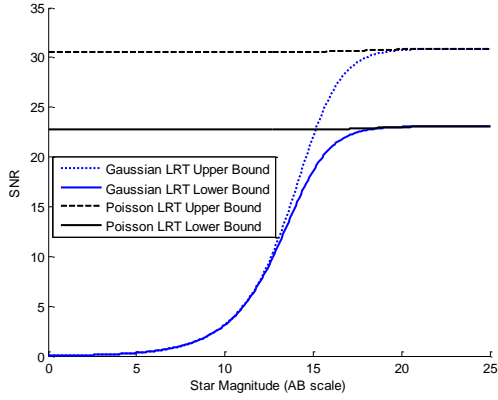14.1 arc-sec Angular Separation

Figure 9. SNR of 400 m NEO vs. Star Mag;
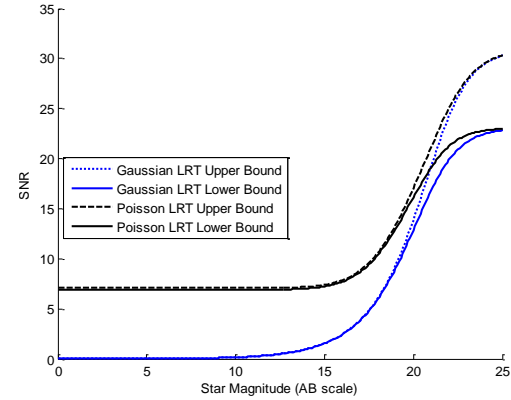
28.2 arc-sec Angular Separation

Figure 10. SNR of 400 m NEO vs. Star Mag; 0

arc-sec Angular Separation

NEO is 140 meters in diameter, and the angular separation between the star and the NEO

is approximately 28.21 arc-seconds. The star's apparent magnitude was varied from 0 to

25. Figure 8 shows a similar set-up where the only change is the angular separation to

around 14.11 arc-seconds. Figure 9 increases the size of the NEO to 400 meters in

diameter, at an angular separation of 28.21 arc-seconds. Since the SNR for such a large

NEO is so large when far enough away from a nearby star, Figure 10 shows the predicted

SNR when the 400 meter diameter NEO is in the same pixel as a background star, or an

angular separation of zero arc-seconds. These results predict that in a flat, dim background the two LRTs should perform equally as well, but the proposed Poisson-based LRT should outperform the Gaussian-based LRT when there is a bright object nearby and the background is not flat. Chapter 3.5 established that using the GLRT could not be analyzed using SNR calculations. The next section will verify the results predicted with the SNR analysis as well as investigate the performance of the GLRT through simulations.

4.3   Simulation Results

The simulated PSF for each of the four wavelengths used to represent Pan-Starrs' wideband filter is shown in Figure 11. The wavelength dependent PSFs were simulated using a r_0 of 8 cm. These PSFs were used to simulate images for testing the performance of each algorithm. Simulated images were created by convolving the four PSFs with the object, adding the four resulting images together, and adding Poisson random noise. Both the Gaussian and the Poisson LRT require the use of the PSF, for this parameter the
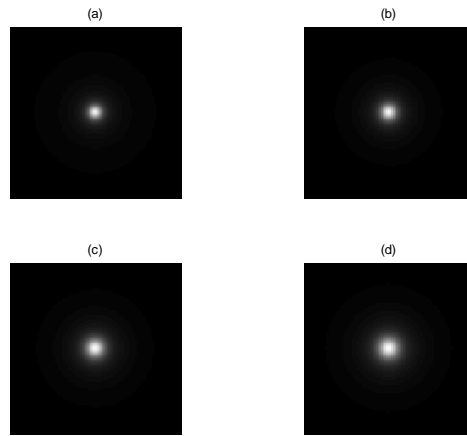

Figure 11. Impulse Response for (a) 500 nm, (b) 600

nm, (c) 700nm, and (d) 800 nm wavelengths

53

average of the four wavelength-dependent PSFs is used. In all Monte Carlo simulations, the NEO was modeled at a distance of 1.3 AUs

Figure 12 shows the ROC curves generated with a Magnitude 20 star, 28.21 arc-seconds away from a 140 meter NEO. These simulated ROC curves support the analytically predicted performance of the two LRTs with a dim star in the background, where they both perform equally as well. Also in Figure 12 is verification that for dim background stars, the performance of the Poisson-based GLRT where the unknown
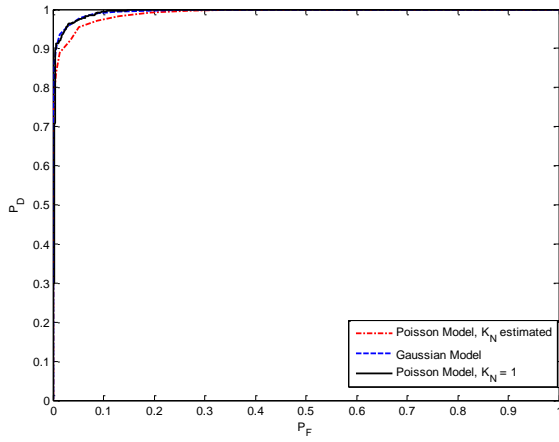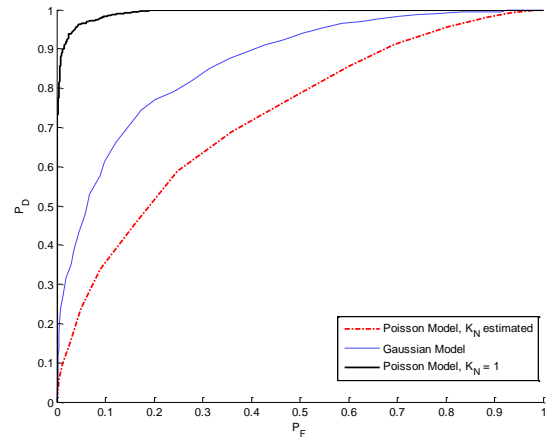

Figure 12. ROC Curve; Magnitude 20 Star

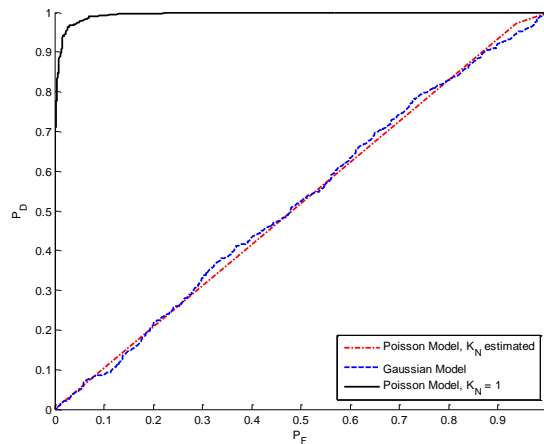Figure 13. ROC Curve; Magnitude 10 Star

Figure 14. ROC Curve; Magnitude 0 star

54

parameter $\bar{K}_N$ is estimated is nearly equivalent to the other two LRTs. If the apparent

magnitude of the star in the background is decreased, making it brighter, the performance

of the Gaussian-based LRT should degrade, according to analytical results. Also, the

performance of the Poisson-based GLRT should degrade due to the increased variance

from the maximum likelihood estimate as discussed in Chapter 3.5. Figure 13 and Figure

14 demonstrate this phenomenon with the simulated ROC curves for the same NEO at the

same angular separation, but with a Magnitude 10 and Magnitude 0 star, respectively.

Figure 15 is a plot of the detection probability versus the apparent magnitude of

the NEO. The NEO magnitude was varied from 21.79 (400 m diameter) to 24.8 (100 m

diameter), the false alarm rate was set to 1×10^{-4}, and the detection probability was

calculated using 1000 simulated realizations of images with Poisson noise. There was no

star simulated in the scene, only background radiation. Figure 15 shows there is nearly a

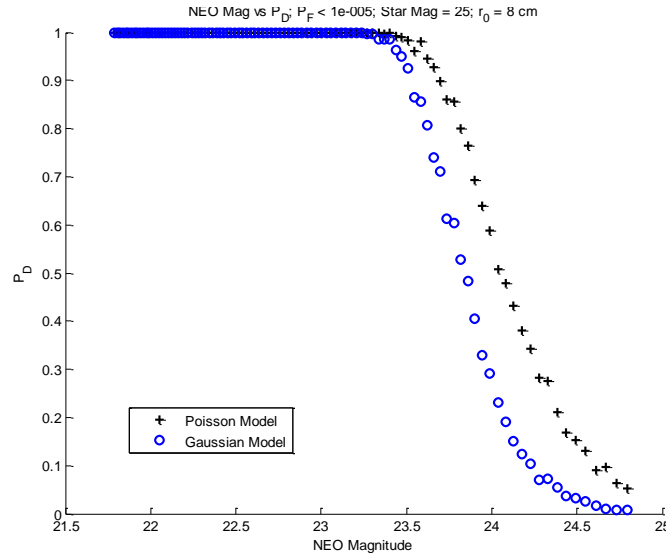doubling in the detection probability for a magnitude 24 NEO, from 0.291 to 0.589.

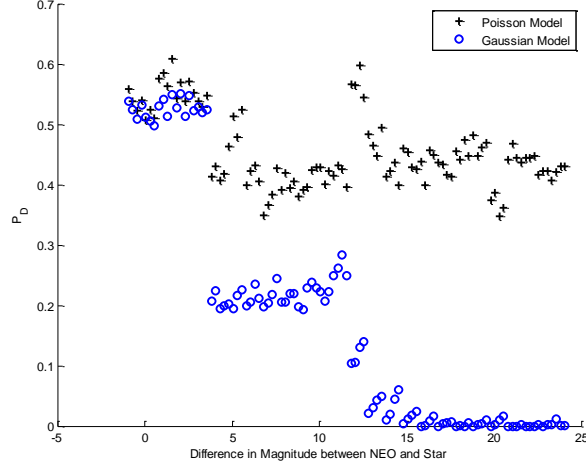Figure 15. Detection Probability vs. NEO Magnitude

Figure 16. Detection Probability vs. NEO-Star magnitude difference

Figure 16 is a plot of the detection probability versus the difference in magnitude between the simulated NEO and the simulated star at an angular distance of 28.21. The magnitude of the NEO was held constant at 24, while the magnitude of the star was varied from 0 to 25. Note that a difference of 5 in apparent magnitude equates to a difference in relative brightness of a factor of 100. Figure 16 shows that the detection probability is marginally improved by the proposed algorithm when the magnitude of the star is less than 100 times as bright as the NEO. When the magnitude of the star is between 100 times and roughly 25,000 times as bright as the NEO, the detection probability is approximately doubled by the proposed algorithm. When the magnitude of the star is greater than roughly 25,000 times as bright as the NEO, the improvement in detection probability by the proposed algorithm is over a factor of 4. A star that is 25,000 times as bright as a NEO may sound like an unlikely encounter, but this is only a difference in magnitude of 11, and in this example the star's magnitude is 14. There are 15.5 million stars as bright as or brighter than a magnitude 14.
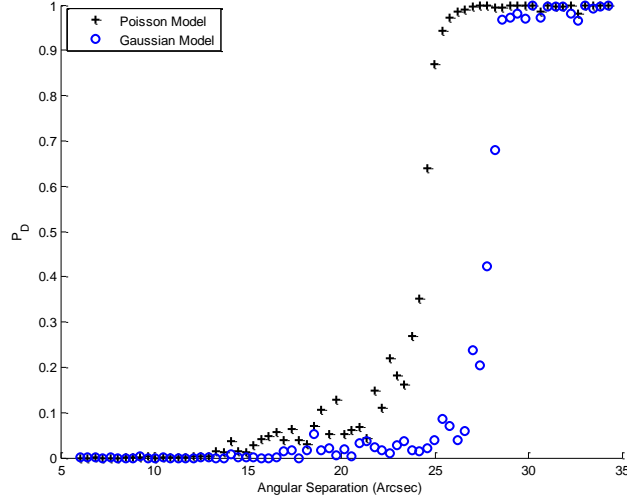
Figure 17. Detection Probability vs. Angular Separation

The final simulated environment varied the angular separation of a 200 meter diameter NEO and a magnitude 15 star from 0 to 28.21 arc-seconds. Again, the detection threshold in this simulation was set to provide a false alarm rate of 1×10^{-4}. Figure 17 is a plot of detection probability versus angular separation and shows that a NEO of this size can be detected with a probability greater than 0.9 approximately 3 arc-seconds closer to a magnitude 15 star with the proposed Poisson-based algorithm than with the current Gaussian-based algorithm.

4.4   Measured Data Results

Two sets of measured data were collected on two different nights with two different CCDs. The first set of data was taken in early August in Dayton, OH. The telescope was brought into focus, and the viewfinder was calibrated using the moon as a reference due to the ease with which the moon is located with an un-calibrated viewfinder. Polaris was then located and its identification was verified by its relative location to the group of stars in the constellation Ursa Major, known as the Big Dipper, as
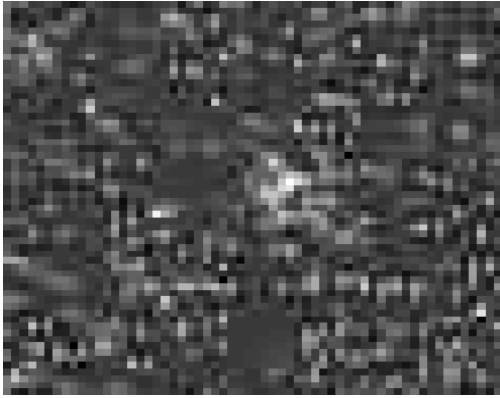
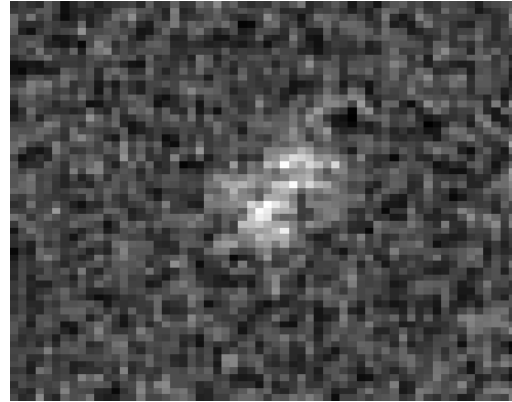Figure 18. Sample image of Polaris with short

exposure

Figure 19. Average Image of Polaris

well as by its stationary location relative to the rotation of the Earth. Once Polaris was

lined up, 347 images were taken at a 1 second exposure time. These long exposures were

used to estimate the average PSF of the telescope and CCD. The integration time of the

CCD was then reduced to $10\,\mu s$, the point at which Polaris was difficult to detect, and

253 images were taken before hardware malfunctions prevented further data collection

for this test. The gain factor was calculated by subtracting the average background noise

from each image and creating an average "super-pixel" around the location of Polaris in

the image. The mean and variance of this super-pixel was then used to calculate the

estimated gain factor of 0.7103, indicating that this particular CCD is not operating in

avalanche mode, and it takes more than one photon to produce an electron. This gain

factor was removed from the data. Figure 18 shows a sample image taken with the

integration time of the CCD set to $10\,\mu s$. Figure 19 shows the average of the 253 images

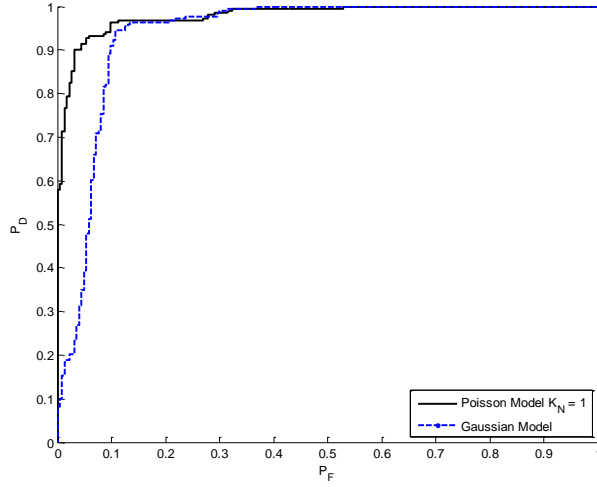taken at that exposure time, and indicates the presence of Polaris.

Figure 20. ROC Curve for Polaris Short Exposure Images

Figure 20 shows the ROC curve developed by using the 10 μs exposure images in the two algorithms. As with the simulated data, the test data depicts an increase in performance by using the proposed algorithm. The detection probability with the Poisson-based LRT at the smallest measureable false alarm rate is 0.5785, while the detection probability with the Gaussian-based LRT for the same false alarm rate is 0.0807. Based on this limited sample set, the increase in detection probability for very small false alarm rates is by a factor of seven.

The second set of data was taken in early December in Dayton, OH. The telescope was again brought into focus, and the viewfinder was calibrated using the moon as a reference as with the first data collection. Immediately it was apparent that the seeing parameter on this night was much better than the night of the previous data collection as many more stars were visible that were not visible with the same optics before. A star in the general location of where Polaris should be was focused on that appeared to be stationary with respect to the rotation of the Earth, so it was assumed that

this was Polaris. A series of 46 images at 1 second exposure time and 1179 images at 10 μs exposure times were taken. Once the data was processed, there was doubt that this star was Polaris because there was some steady movement of the star. This required that the images be registered before they could be. Another issue discovered after post-processing the data, was that the long exposure images saturated the CCD, this means that these 46 images were not the shape of the PSF. Instead the cross-section of the intensity of these images resembled what is commonly referred to as a "Top-Hat" function where the top portion of the image intensity data was cut off. These images were used to estimate the PSF by creating a simulated PSF that had the same shape and width as the base of the average of these 46 images. In a similar manner as with the first set of data, the estimated gain factor was found to be 1.1932, indicating that this CCD is operating in avalanche mode and more than one electron is produced for every photon. This gain factor was removed from the data. Figure 21 shows a sample image taken with the integration time of the CCD set to 10 μs. Figure 22 shows the average of the 1179 images taken at that exposure time, and indicates the presence of the star.
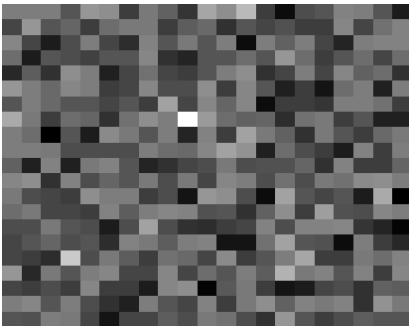

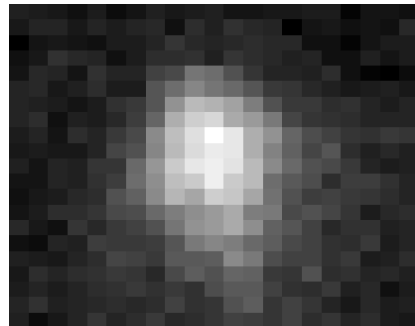Figure 21. Sample Image of Star with Short Exposure
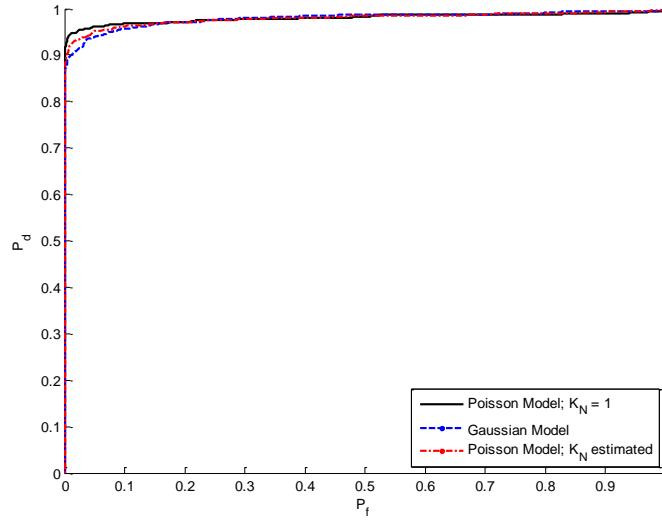

Figure 22. Average Image of Star

Figure 23. ROC Curve of Second Data Set

Figure 23 shows the ROC curve developed by using the $10\,\mu s$ exposure images with the Poisson LRT, the Poisson GLRT, and the Gaussian LRT. The improvement is not as significant as with the first set of data and there are several possible contributing factors for this. The first set of data had a limited number of samples; whereas the second set of data had a much more statistically significantly number of samples, also r_0 on the second night of collection was much better, making the average PSF smaller. The second set of data with more samples more closely resembles the simulated performance of a NEO without the presence of a star nearby. Analysis and simulations done with models of Pan-Starrs predicted the performance of the LRTs and the GLRT should be approximately the same given that Polaris was the only thing in the image. The detection probability with the Poisson LRT at the smallest measureable false alarm rate is 0.9101, while the detection probability with the Gaussian LRT for the same false alarm rate is 0.8117. The nearly 10% increase in probability of detection realized in this data set could

indicate the resilience of the proposed Poisson-based LRT to other sources of noise not accounted for in simulations and SNR analysis. One such source of noise is scintillation in which the PSF fluctuates over time. The 10 μs integration time for the measured data would see a larger fluctuation in the shape of the PSF than the 30 seconds modeled for Pan-Starrs simulations, the PSF of which would more closely resemble the average PSF. Further research is required to definitively characterize the realized improvement in this data set versus the expected performance based on simulations and analysis.

4.5   Summary

This chapter presented the numerical and graphical results of the analysis, simulation, and measurement of the performance of the proposed algorithm in comparison with the existing matched filter, or Gaussian-based algorithm. The results in all cases studied demonstrate an improved performance by the proposed algorithm over the matched filter.

5   Conclusions and Recommendations

5.1   Chapter Overview

This chapter presents conclusions and recommendations derived from performing this research effort. The chapter begins by summarizing conclusions drawn from the results presented in Chapter 4. Next, the significance and impact of the inferred conclusions are projected. Finally, recommendations are made for immediate action and for future work.

5.2   Conclusions of Research

The Poisson-based LRT algorithm proposed by this research produced increases in probability of detection as high as a factor of seven over the existing algorithm for measured data. In all simulated conditions explored, the proposed algorithm performed as well as the current matched filter algorithm. In certain simulated conditions such as a dim NEO near a bright star, the detection rate for small false alarm rates was more than a factor of four. Little has changed in the past few decades with regard to the basic image signal processing theory used in the detection of dim astronomical objects. The optical systems have increasingly become more capable and functional, but how the data received from the optical systems are processed remains fundamentally the same, with the exception of the Pan-Starrs program and the projected LSST program.

5.3   Significance of Research

The significance of this research is potentially very important to the astronomical community. The research demonstrated improvement in binary detection applications through theoretical analysis, simulated hardware used in NEO detection, and with real

images taken with two different cameras on a much smaller telescope than would feasibly be used for NEO detection. This leads to the conclusion that the proposed algorithm has utility across all applications of detecting the presence of any dim astronomical object using terrestrial-based optical systems. Potential significance of the research ranges from an increased capability of tracking debris in orbit, to detecting a previously undetectable asteroid or comet on a collision course with Earth early enough to establish an effective plan of action to save millions of lives.

5.4   Recommendations for Action and Future Research

The research conducted here was unfunded; however, based on preliminary results prior to the completion of this research, interest from one particular survey program was expressed in the potential impacts of this research. There are a few challenges remaining before the proposed algorithm is easily incorporated to existing hardware. A thorough study of calibration issues, hardware specific parameters, and any other engineering challenges in order to optimize the algorithm is required. A method is needed that determines the threshold of detection, which varies from one location in the sky to another due to the background image, and is also hardware specific. Once these challenges are overcome, the research should be extended to measure the actual gain realized on more sophisticated astronomical imaging equipment.

5.5   Summary

In the final chapter, conclusions drawn from the research conducted are presented. Potential significance of the results reported is forecasted and recommendations for actions based on this research as well as future research to be conducted are presented.

Appendix

A1. Simulation MatLab Code

```
%Capt Curtis Peterson MatLab M-Code
%Pan-Starrs model and Simulations

%% Adjustable Parameters
Target_radius = 70;              % NEO radius in meters
trials = 1000;                   % number of trials for Monte Carlo Simulations
rho_t = .03;                     % Target reflectivity
r_0 = 0.08;                      % atmospheric seeing parameter in meters
Star_Mag = 10;                   % Apparent Magnitude (AM) in AB system of nearby star
NEO_position = [15 15];          % Pixel location (x,y) of the NEO
star_position = [85 85];         % Pixel location (x,y) of nearby star
master_images = 100;             %number of images to average for the master image
run_ps1_psf = 0;                 % 1 == run code to develop psf of ps1 (very time
                                 % consuming), 0 == skip this section of code (if you
                                 % have previously run it and saved the psf.mat)
estimate_K_N = 1;                % 1 == run code to estimate the K_N parameter in the
                                 % Poisson LRT, 0 == set K_N equal to 1.

%% Fixed Parameters
M_a = 5123;                      % number of samples in aperture
M_d = 100;                       % number of samples (pixels) in the simulated detector
D = 1.8;                         % diameter of the mirror (aperture) in meters
f = 8;                           % focal length of the system in meters
dx = D/M_a;                      % sample size in the aperture in meters
dy = dx;
dxx = 10e-6;                     % sample size in the detector in meters
dyy = dxx;
AU = 1.495978707e11;             % 1 AU in meters
Target_Range = 1.3*AU;           % range to target in meters (definition of NEO)
h = 6.626e-34;                   % Planck's constant
delta_lam = .1;                  % Bandwidth of receiver in units of micrometers
delta_t = 30;                    % exposure time of PS1 in seconds
K_B = 7;                         % average background photo-electrons per pixel
r1 = M_a/2;
r2 = 0;
total_imp_resp = zeros(M_d,M_d,4);  % allocate space for impulse response
ps1_psf = total_imp_resp;        % allocate space for psf
K_N = zeros(1,4);                % allocate space for expected number of
                                 % photo-electrons received from NEO
vega = [5.53215e11 5.1066e11 4.72506e11 4.38756e11]; %photons received by
                                 %1.8 m aperture from
                                 %Vega per wavelength
K_S = vega/(2.512^Star_Mag);     %photo-electrons received from nearby star per
                                 %wavelength
angluar_separation = norm(star_position-NEO_position)*0.285; %star to NEO
                                 %separation in arc-seconds
for wavelength = 1:4;
%% Create Impulse Response
    % select the wavelength dependent parameters
```

```matlab
    if wavelength == 1
        lam = 0.5e-6;                  %wavelength in meters
        S_irr = 2e3;                   %solar spectral irradiance (W/m/um)
        tau_opt = 0.67;                %optical transmittance of ps1
        tau_atm = .98;                 %atmospheric optical transmittance
    elseif wavelength == 2
        lam = 0.6e-6;
        S_irr = 1.8e3;
        tau_opt = 0.85;
        tau_atm = .99;
    elseif wavelength == 3
        lam = 0.7e-6;
        S_irr = 1.4e3;
        tau_opt = 0.99;
        tau_atm = .9;
    else lam = 0.8e-6;
        S_irr = 1e3;
        tau_opt = 0.95;
        tau_atm = .9;
    end

if run_ps1_psf==1
    %create M_a by M_a aperture array with a circular binary screen equal to the
    %size of the mirror
    mi = floor(r1) + 1;
    aperture_array = zeros(M_a,M_a);
        for ii = 1:M_a
            for jj = 1:M_a
                dist = sqrt((ii-mi)^2+(jj-mi)^2);
                if(dist <= r1)
                    if(dist >= r2)
                        aperture_array(ii,jj)=1;
                    end
                end
            end
        end
    x = dx*(-floor(r1):floor(r1));
    xx_mat = ones(M_a,1)*x;        %create matrices for vectorizing the
                                   %lens phase and field propagation
                                   %math in the next two steps

    yy_mat = x'*ones(1,M_a);
    %Treat the telescope as a single thin lens with focal length f and
    %apply the lens phase to the aperture
    lens_phase = -pi*(xx_mat.^2 + yy_mat.^2)/(f*lam);
    source_array = aperture_array.*exp(1j.*lens_phase);
    %Propagate the aperture field to the receiver array using the
    %Rayleigh-Sommerfeld diffraction integral
    receiver_array = zeros(M_d,M_d);
        for xx = 1:M_d
            xxc = (xx - ceil(M_d/2))*dxx;
            for yy = 1:M_d
                yyc = (yy - ceil(M_d/2))*dyy;
                R = (f^2 + (xx_mat-xxc).^2 + (yy_mat-yyc).^2).^(0.5);
```

```matlab
            receiver_array(yy,xx) = sum(sum(dx*dy*source_array.*...
                exp(2*pi*1j.*R./lam)))./(lam*1j*f);
        end
      end
    %find the point spread function  of PS1, which is normalized
    ps1_psf(:,:,wavelength) = abs(receiver_array).^2;
    ps1_psf(:,:,wavelength) = ps1_psf(:,:,wavelength)/...
                  sum(sum(ps1_psf(:,:,wavelength)));
  end
   % Find the average atmospheric transfer function for a long exposure
   % and multiply it by the transfer function of PS1 in order to get the
   % total transfer function.  Take the inverse Fourier transform of the
   % total transfer function in order to find the total impulse response
  dx_otf = lam*f/(M_d*dxx);
  avg_otf = zeros(M_d,M_d);
  mii = floor(M_d/2)+1;
  for i = 1:M_d
    for j = 1:M_d
      dist = sqrt((i-mii)^2+(j-mii)^2);
      if(dist<=2*(D/2)/dx_otf)
        avg_otf(i,j)=exp(-3.44*((dist/(r_0/(dx_otf)))^(5/3)));
      end
    end
  end
  tot_otf = fftshift(avg_otf).*(fft2(fftshift(ps1_psf(:,:,wavelength))));
  total_imp_resp(:,:,wavelength) = abs(ifftshift(ifft2(tot_otf)));

%%% Calculate Expected number of photons from NEO for each wavelength
  v = 3e8/lam;                    %frequency
  %dA is the smallest of the IFOV and the area of the target
  IFOV = (dxx/f*Target_Range)^2;
  A_B = Target_radius^2*pi;
  if IFOV < A_B
    dA = IFOV;
  else
    dA = A_B;
  end

  K_N(wavelength) = S_irr*delta_lam*dA*rho_t*tau_atm*tau_opt*D^2*...
        delta_t/(4*Target_Range^2*h*v);
end
%%% SNR Calculations
%the following variables and expressions occur in the SNR calculations
psf_avg = mean(total_imp_resp,3);   % average, non-wavelength dependent psf
R_h = max(max(xcorr2(psf_avg)));    % zero lag auto correlation of psf
KN = sum(K_N);      %total expected photo-electrons from NEO
IM_h2 = sum(sum(I_M.*(circshift(psf_avg,NEO_position-50).^2)));
h2_IM = sum(sum((circshift(psf_avg,NEO_position-50).^2)./I_M));
KN_h3 = sum(sum(KN*psf_avg.^3));
h3_IM = sum(sum((KN*circshift(psf_avg,NEO_position-50).^3)./(I_M.^2)));
Var_Gaus_H1 = KN_h3 + IM_h2;
Var_Gaus_H0 = IM_h2;
Var_Pois_H1 = h3_IM + h2_IM;
```

```matlab
Var_Pois_H0 = h2_IM;
SNR_Gaus_upper(NEOsize,starsize) = (KN*R_h)/sqrt(Var_Gaus_H0);
SNR_Gaus_lower(NEOsize,starsize) = (KN*R_h)/sqrt(Var_Gaus_H1);
SNR_Pois_upper(NEOsize,starsize) = (KN*h2_IM)/sqrt(Var_Pois_H0);
SNR_Pois_lower(NEOsize,starsize) = (KN*h2_IM)/sqrt(Var_Pois_H1);


%% Find Probabilities of detection and Probabilities of false alarm for the
%given NEO Magnitude, Star Magnitude, Angular Separation
NEO_mag = log(sum(vega)/sum(K_N))/log(2.512); %Apparent Magnitude of NEO
NEO = zeros(M_d,M_d,4);
NEO(NEO_position(1),NEO_position(2),:) = K_N;


%conv2 is used below to create the image of the NEO (similarly to create the
%image of the star) though the PS1 optics as opposed to using fft2 due to the
%periodicity of the fft2 function which caused edge effects and inaccurate
%results when either the star or the NEO was placed close to the edge of the
%simulated image
NEO_image = conv2(NEO(:,:,1),total_imp_resp(:,:,1),'same') + ...
   conv2(NEO(:,:,2),total_imp_resp(:,:,2),'same') + ...
   conv2(NEO(:,:,3),total_imp_resp(:,:,3),'same') + ...
   conv2(NEO(:,:,4),total_imp_resp(:,:,4),'same');

[col row] = find(NEO_image==max(max(NEO_image)));

if estimate_K_N == 0;
   eta_pois = 0:1e-4:3; %Poisson LRT range of thresholds
elseif estimate_K_N == 1;
   eta_pois = [0:.001:10 10:.1:100 100:1000 1e3:10:1e4 1e4:1e2:1e5 ...
      1e5:1e3:1e6 1e6:1e4:1e7];
end


 eta_gaus = -100+200/length(eta_pois):...
         200/length(eta_pois):100; %Gaussian LRT range of thresholds
det_pois = zeros(length(eta_pois),trials);
fa_pois = det_pois;
fa_gaus = det_pois;
det_gaus = det_pois;

star = zeros(size(total_imp_resp));
star(star_position(1),star_position(2),:) = K_S;

star_image = conv2(star(:,:,1),total_imp_resp(:,:,1),'same') + ...
   conv2(star(:,:,2),total_imp_resp(:,:,2),'same') + ...
   conv2(star(:,:,3),total_imp_resp(:,:,3),'same') + ...
   conv2(star(:,:,4),total_imp_resp(:,:,4),'same');
I_M = (star_image + K_B);


%the variable fx below is a fixed value for all trials and is placed outside of the for loop
%of trials below in order to reduce run time
fx= circshift(psf_avg,[col-50 row-50])./I_M;

for trial = 1:trials;
```

68

```matlab
    d_0 = poissrnd(I_M);                % noisy image data with H0
    d_1 = poissrnd(I_M + NEO_image);    %noisy image data with H1
    if estimate_K_N == 1;
       K_N_hat_H0 = sum(sum((d_0-I_M).*((d_0-I_M)>0)));
       K_N_hat_H1 = sum(sum((d_1-I_M).*((d_1-I_M)>0)));
    elseif estimate_K_N == 0;
       K_N_hat_H0 = 1;
       K_N_hat_H1 = 1;
    end

%calculate the Poisson LRT values for both hypotheses
        Poisson_LRT_H1 = sum(sum((d_1/ K_N_hat_H1) .* log(1 + K_N_hat_H1*fx)));
        Poisson_LRT_H0 = sum(sum((d_0 / K_N_hat_H0).* log(1 + K_N_hat_H0*fx)));
%calculate the Gaussian LRT values for both hypotheses
   Gaussian_LRT_H0 = conv2(d_0-I_M,psf_avg,'same');
   Gaussian_LRT_H0 = Gaussian_LRT_H0(col-1,row-1);

   Gaussian_LRT_H1 = conv2(d_1-I_M,psf_avg,'same');
   Gaussian_LRT_H1 = Gaussian_LRT_H1(col-1,row-1);
 %determine false alarms and detections for the range of thresholds
    for k = 1:length(eta_pois)
       fa_gaus(k,trial) = Gaussian_LRT_H0 >= eta_gaus(k);
       det_gaus(k,trial) = Gaussian_LRT_H1 >= eta_gaus(k);
       fa_pois(k,trial) = Poisson_LRT_H0 >= eta_pois(k);
       det_pois(k,trial) = Poisson_LRT_H1 >= eta_pois(k);
    end
end
%Calculate the Probabilities of False Alarm and Detection for the given
%number of trials
Pd_Pois = sum(det_pois,2)/trials;
Pd_Gaus = sum(det_gaus,2)/trials;
Pfa_Pois = sum(fa_pois,2)/trials;
Pfa_Gaus = sum(fa_gaus,2)/trials;
exit
```

A2. Measured Data MatLab Code

```
%Capt Curtis Peterson
%Thesis Measured Data MatLab M-code
%Compare Poisson Based LRT to Gaussian Based LRT with images of Polaris
%taken at a 10us exposure time.

estimate_K_N = 1; %choose whether to estimate the value of K_N
                    %(1==estimate)

%%% Import .jpg image data (modify for other image formats)

%Create NxMxdummy array "A" which is an array of registered and %resolved two dimensional
intensity images of Polaris from a long %integration time. This will be used to estimate the PSF of the
%telescope.
psf_jpegs = dir(['<filename>','*.jpg']);
[N,M,dummy]=size(imread(psf_jpegs(1).name));
psf_numfiles = length(psf_jpegs);
A = zeros(N,M,psf_numfiles);

for k = 1:psf_numfiles
  I = imread(psf_jpegs(k).name);
  I = mean(I,3);
  A(:,:,k) = mat2gray(I);
end

%Create N1xM1xdummy1 array "images" which is an array of registered %unresolved two
dimensional intensity images of Polaris from a short %integration time. This will be used as a noisy
data image for LRT %detection
images_jpegs = dir(['<filename>','*.jpg']);
[N1,M1,dummy1]=size(imread(images_jpegs(1).name));
images_numfiles = length(images_jpegs);
images = zeros(N,M,images_numfiles);

for k = 1:images_numfiles
  I1 = imread(images_jpegs(k).name);
  images(:,:,k)=mean(I1,3);
end

%%% Estimate the telescope PSF

%find the max of the average PSF and shift it to the zero lag, or the
%center of the image, then create a 40x40 image of the PSF less the average
%background noise, and normalize it, this is the estimated PSF.  A 40x40
%array is used because that is the size of the region of the image that
%will be searched for an "object" (Polaris) from the noisy data images
average_psf = mean(A,3); %the average resolved image of Polaris has the
              %general shape of the PSF
m=max(max(average_psf));
[col,row]=find(average_psf==m);
shiftR = N/2 - col + 1;
shiftD = M/2 - row + 1;
avg_noise = mean2(average_psf(:,1:row-100));
```

```
psf_temp = circshift(average_psf,[shiftR,shiftD]);
psf_test = psf_temp(N/2-20:N/2+19,M/2-20:M/2+19);
psf_test = (psf_test - avg_noise).*((psf_test - avg_noise)>0);
psf_test = psf_test/max(max(psf_test));

%find the location of Polaris in the noisy data set by averaging them
%together and finding the peak.  A 40x40 region around the location of
%Polaris will be used as the search region
average_image = mean(images,3);
m1=max(max(average_image));
[col1,row1]=find(average_image==m1);

shift_a = col1 - 20:col1 + 19;
shift_b = row1 - 20:row1 + 19;

%%% Calculate the CCD Gain factor

% the gain factor is estimated as the average gain over the 40 pixels
% of interest which is the mean over all the images of the average
% value of the 40x40 pixels minus the mean background noise for the
% same pixels divided by the variance of the same
images1=mean(mean(images(shift_a,shift_b,:),1),2);
for k = 1:images_numfiles
   noise(k)=mean2(images(:,1:row1 - 100,k));
end
images2(1,:) = images1(1,1,:);
images2 = images2 - noise;
Gain = mean(images2)./var(images2);
images = images.*Gain;

%%% Calculate the Poisson and Gaussian LRTs for H1 and H0

Poisson_LRT_H1 = zeros(length(shift_a),length(shift_b),size(images,3));
   Poisson_LRT_H0 = Poisson_LRT_H1;
   Gaussian_LRT_H1 = zeros(1,size(images,3));
   Gaussian_LRT_H0 = Gaussian_LRT_H1;
   Poisson_LRT_H1_Max = Gaussian_LRT_H1;
   Poisson_LRT_H0_Max = Gaussian_LRT_H1;

for im_num = 1:size(images,3)

   d_1 = images(shift_a,shift_b,im_num); %data for H1 for image number
                                         %im_num
   d_0 = images(shift_a + 150,shift_b - 150,im_num); %data for H0 for
                                         %image number im_num, using
                                         %background noise from some
                                         %offset from the location of %Polaris
   I_M = mean2(d_0)*ones(size(d_0)); %the "master Image" is a constant
                   %equal to the average background
                   %noise
   if estimate_K_N == 1;
      K_N_hat_H0 = sum(sum((d_0-I_M).*((d_0-I_M)>0)));
      K_N_hat_H1 = sum(sum((d_1-I_M).*((d_1-I_M)>0)));
```

71

```matlab
    elseif estimate_K_N == 0;
       K_N_hat_H0 = 1;
       K_N_hat_H1 = 1;
    end
       for alpha = 1:length(shift_a);
          for beta = 1:length(shift_b);
             %shift the PSF through every pixel in the image,
                         %calculate the LRT and then find the max value of the
                         %LRT and compare it to a threshold
             f = (circshift(psf_test,...
                [shift_a(alpha)-20 shift_b(beta)-20])),/I_M;
             Poisson_LRT_H1(alpha,beta,im_num) = sum(sum((d_1/K_N_hat_H1).*...
                         log(1+K_N_hat_H1*f)));

             Poisson_LRT_H0(alpha,beta,im_num) = sum(sum((d_0/K_N_hat_H0).*...
                         log(1+K_N_hat_H0*f)));
          end
       end
       %max Pois LRT value for H1 data:
     Poisson_LRT_H1_Max(im_num) =max(max(Poisson_LRT_H1(:,:,im_num)));

       %max Pois LRT value for H0 data, and estimating G:
     Poisson_LRT_H0_Max(im_num) = max(max(Poisson_LRT_H0(:,:,im_num)));

       %max Gaus LRT value for H1 data:
     Gaussian_LRT_H1(im_num)=max(max(conv2((d_1-I_M),psf_test,'same')));

       %max Gaus LRT value for H0 data:
     Gaussian_LRT_H0(im_num)=max(max(conv2((d_0-I_M),psf_test,'same')));
end
eta_gaus = 0:.1:6000; %range of threshold for Gaussian LRT
if estimate_K_N == 0;
  eta_pois = 240:140/length(eta_gaus):380-140/length(eta_gaus);
                                                %Poisson LRT range of %thresholds
elseif estimate_K_N == 1;
  eta_pois = 1.2e5:3e5/length(eta_gaus):4.51e5-3e5/length(eta_gaus);
                                                %range of threshold for %Poisson LRT
                                                with K_N %estimated
end

%allocate space for probabilities of detection & false alarms for all %tests
pd = zeros(1,length(eta_gaus));
pfa = pd;
pd_g = pd;
pfa_g = pd;
%compare peak detection of the tests to a varying threshold to build a
%ROC curve
for k = 1:length(eta_gaus)
 pd(k)=sum(Poisson_LRT_H1_Max>eta_pois(k))/length(Poisson_LRT_H1_Max);
 pfa(k)=sum(Poisson_LRT_H0_Max>eta_pois(k))/length(Poisson_LRT_H0_Max);
 pd_g(k) = sum(Gaussian_LRT_H1>eta_gaus(k))/length(Gaussian_LRT_H1);
 pfa_g(k) = sum(Gaussian_LRT_H0>eta_gaus(k))/length(Gaussian_LRT_H0);
end
```

Bibliography

1. **Congress, United States 109th.** *Public Law 109–155.* s.l. : United States Government, 2005. United States Legislation.

2. **National Aeronautics and Space Administration.** *Spaceguard Survey; Asteroid and Comet Impact Hazards.* s.l. : United States Government, 1992. Survey.

3. —. *Near-Earth Object Survey and Deflection Analysis of Alternatives Report to Congress.* 2007.

4. —. *Study to Determine the Feasibility of Extending the Search for Near-.* 2003.

5. —. NASA Budgets and Plans. *NASA.* [Online] [Cited: July 25, 2011.] http://www.nasa.gov/pdf/428154main_Planetary_Science.pdf.

6. —. NEO Discovery Statistics. *Near Earth Objects Program.* [Online] [Cited: January 5, 2012.] http://neo.jpl.nasa.gov/stats/.

7. **University of Arizona.** SpaceWatch. [Online] [Cited: 08 09, 2011.] http://spacewatch.lpl.arizona.edu/index.html.

8. **Stokes, Grant H., Evans, Jenifer B. and Larson, Stephen M.** *Near-Earth Asteroid Search Programs.* s.l. : University of Arizona Press and the Lunar and Planetary Institute.

9. **National Aeronautics and Space Administration.** Near Earth Object Program. *NASA.* [Online] [Cited: 08 14, 2011.] http://neo.jpl.nasa.gov/programs/.

10. **LSST Corporation.** Large Synoptic Survey Telescope. *LSST REFERENCE DESIGN.* [Online] 06 04, 2011. [Cited: 08 14, 2011.] http://www.lsst.org/files/docs/overviewV2.0.pdf. arXiv:0805.2366 Version 2.0.9.

11. Pan-Starrs. [Online] 2005. [Cited: 03 02, 2011.] http://pan-starrs.ifa.hawaii.edu/public/.

12. **Magnier, Eugene.** PSPhot Sofware Design Description, The Pan-STARRS IPP Object Photometry Tool. *University of Hawaii at Manoa.* [Online] 2007. [Cited: 08 14, 2011.] http://ipp0222.ifa.hawaii.edu/ippData/manuals/psphot.pdf. PSDC-430-021-DR.

13. **Gural, Peter S., Larsen, Jeffrey A. and Gleason, Arianna E.** Matched Filter Processing for Asteroid Detection. *The Astronomical Journal.* 2005, Vol. 130, 4.

14. *Likelihood-Based Method for Detecting Faint Moving Objetcs.* **Miura, Noriaki, Itagaki, Kazuyuki and Baba, Naoshi.** 3, s.l. : The Astronomical Journal, 2005, Vol. 130. doi:10.1086/431955.

15. **O'Dell, Anthony.** *Detecting Near-Earth Objects Using Cross-Correlation With A Point Spread Function.* Wright Patterson AFB, OH : Air Force Institute of Technology, 2009. AFIT/GE/ENG/09-30.

16. **Richmond, Richard D. and Cain, Stephen C.** *Direct-Detection LADAR Systems.* Bellingham, Washington : SPIE, 2010. 978-0-8194-8072-9.

17. **Alliss, Randall J. and Felton, Billy D.** *Validation of Optical Turbulence Simulation from a Numerical Weather Prediction Model in Support of Adaptive Optics Design.* Chantilly, VA : Northrop Grumman Information Systems/TASC.

18. **Goodman, Joseph W.** *Statistical Optics.* New York : John Wiley & Sons, 1985. 0-471-01502-4.

19. **Thomas, George B., Jr. and Finney, Ross L.** *Calculus and Analytic Geometry, 9th Edition.* Reading, Massachusetts : Addison-Wesley Publishing Company, 1996. 0-201-53174-7.

20. **Kay, Steven.** *Intuitive Probability and Random Processes Using MATLAB.* New York : Springer Science+Business Media, Inc., 2006. 978-0-387-24157-9.

21. **Rohde, Robert A.** *Solar Radiation Spectrum.* Global Warming Art, s.l. : s.n.

22. **Christopher W. Stubbs, Peter Doherty, Claire Cramer,Gautham Narayan, Yorke J. Brown.** Precise Throughput Determination of the PanSTARRS Telescope and the Gigapixel Imager using a Calibrated Silicon Photodiode and a Tunable Laser: Initial Results. *Cornell University Library.* [Online] 03 17, 2010. [Cited: 03 02, 2011.] http://arxiv.org/abs/1003.3465v1.

23. **Hecht, Eugene.** *Optics, 4th Edition.* San Francisco : Pearson Education, Inc., 2002. 0-8053-8566-5.

24. **Kay, Steven M.** *Fundamentals of Statistical Signal Processing-Volume 1 Estimation Theory.* Castleton, NY : Prentice-Hall, Inc., 2010. 0-13-345711-7.

25. **Hardy, John W.** *Adaptive optics for astronomical telescopes (page 92).* s.l. : Oxford University Press, 1998. 9780195090192.

26. **Goodman, Joseph W.** *Introduction to Fourier Optics.* Greenwood Village, CO : Roberts & Company Publishers, 2005. 0-9747077-2-4.

1. REPORT DATE (DD-MM-YYYY) 22-03-2012	2. REPORT TYPE Master's Thesis	3. DATES COVERED (From – To) August 2010 – March 2012

TITLE AND SUBTITLE		5a. CONTRACT NUMBER
Near Earth Object Detection Using C Poisson Statistical Model For Detection On Images Modeled From The Panoramic Survey Telescope & Rapid Response System		
		5b. GRANT NUMBER
		5c. PROGRAM ELEMENT NUMBER

6. AUTHOR(S)	5d. PROJECT NUMBER
Peterson, Curtis J. R., Captain, USAF	
	5e. TASK NUMBER
	5f. WORK UNIT NUMBER

7. PERFORMING ORGANIZATION NAMES(S) AND ADDRESS(S) Air Force Institute of Technology Graduate School of Engineering and Management (AFIT/ENG) 2950 Hobson Way, Building 640 WPAFB OH 45433-8865	8. PERFORMING ORGANIZATION REPORT NUMBER AFIT/GE/ENG/12-33

9. SPONSORING/MONITORING AGENCY NAME(S) AND ADDRESS(ES) Air Force Research Laboratory Detachment 15 535 Lipoa Pkwy Ste 200 Kihei, HI 96753 (808) 891-7762 POC: Mark Bolden; mark.bolden@maui.afmc.af.mil	10. SPONSOR/MONITOR'S ACRONYM(S) AFRL/RDSM
	11. SPONSOR/MONITOR'S REPORT NUMBER(S)

12. DISTRIBUTION/AVAILABILITY STATEMENT
APPROVED FOR PUBLIC RELEASE; DISTRIBUTION UNLIMITED.

13. SUPPLEMENTARY NOTES
This material is declared a work of the U.S. Government and is not subject to copyright protection in the United States.

14. ABSTRACT:
The purpose of this research effort is to develop, simulate, and test a new algorithm to detect Near Earth Objects (NEOs) using a Likelihood Ratio Test (LRT) based on a Poisson statistical model for the arrival of photons. One detection algorithm currently in use is based on a Gaussian approximation of the arrival of photons, and is compared to the proposed Poisson model. The research includes three key components. The first is a quantitative analysis of the performance of both algorithms. The second is a system model for simulating detection statistics. The last component is a collection of measured data to apply comparatively to both algorithms.

A Congressional mandate directs NASA and the DoD to catalogue 90% of all NEOs by the year 2020. [1] Results from this research effort could feasibly be applied directly to operations in the Pan-Starrs program to facilitate the accomplishment of the Congressional mandate. Improvements in the size of detectable NEOs and in the probability of detecting larger NEOs would increase the state of readiness of the world for possible catastrophic impact events. Improvements in detection probability of measured data were as high as a factor of seven, and the expected average improvement is around 10%.

15. SUBJECT TERMS
NEO Detection; Astronomical Image Processing

16. SECURITY CLASSIFICATION OF:			17. LIMITATION OF ABSTRACT	18. NUMBER OF PAGES	19a. NAME OF RESPONSIBLE PERSON Stephen Cain, PhD (ENG)
a. REPORT	b. ABSTRACT	c. THIS PAGE	UU	87	19b. TELEPHONE NUMBER (Include area code) (937) 255-3636, ext 4716 (Stephen.cain@afit.edu)
U	U	U			